HYDROTHERMAL SYNTHESIS OF MnO2 NANOPARTICLES INCORPORATED MoS2 NANOFLOWERS FOR EXCEPTIONALLY STABLE SUPERCAPACITOR ELECTRODE

A thesis submitted to the

Department of Materials and Metallurgical Engineering (MME)

of

Bangladesh University of Engineering and Technology (BUET)

In partial fulfillment of the requirement for the degree of

MASTER OF SCIENCE IN MATERIALS AND METALLURGICAL ENGINEERING

By

Md.Roxy Islam

Roll No. 0421112022

MASTER OF SCIENCE IN MATERIALS AND METALLURGICAL ENGINEERING

Department of Materials and Metallurgical Engineering

BANGLADESH UNIVERSITY OF ENGINEERING AND TECHNOLOGY

May,2023

The thesis titled" HYDROTHERMAL SYNTHESIS OF MnO2 NANOPARTICLES INCORPORATED MoS2 NANOFLOWERS FOR EXCEPTIONALLY STABLE SUPERCAPACITOR ELECTRODE " Submitted by Md.Roxy Islam , Roll No: 0421112022, Session: April-2021 has been accepted as satisfactory in partial fulfillment of the requirement for the degree of Master of Science in Materials and Metallurgical Engineering on 24.05.2023.

BOARD OF EXAMINERS

24.05.2023

Dr. Md. Muktadir Billah Associate Professor Department of Materials and Metallurgical Engineering, BUET, Dhaka	Chairman (Supervisor)
25/5/2023 Dr. A.K.M. Bazlur Rashid Professor & Head Department of Materials and Metallurgical Engineering, BUET, Dhaka	Member (Ex-Officio)
Dr.Fahmida Gulshan Professor Department of Materials and Metallurgical Engineering, BUET, Dhaka	Member
Dr. Ahmed Sharif Professor Department of Materials and Metallurgical Engineering, BUET, Dhaka	Member
Dr. Muhammad Rakibul Islam Professor Department of Physics, BUET, Dhaka	Member (external)

CANDIDATE'S DECLARATION

It is hereby declared that this thesis or any part of it has not been submitted elsewhere for the award of any degree or diploma.

Md.Roxy Islam

DEDICATION

I owe it to my Creator (Allah Subhanahu Wa Ta'ala), who endowed me with an inquisitive intellect, to satiate that curiosity.

For my dear parents.

Acknowledgments

I want to dedicate all the glory to the Almighty Allah, who has given me the ability and the chance to finish my thesis. My deepest appreciation and admiration go out to Dr. Md. Muktadir Billah, Associate Professor in the Department of Materials and Metallurgical Engineering at Bangladesh University of Engineering and Technology (BUET), for his guidance, patience, and support during my research work. I want to express my gratitude for his generosity with his time in particular. It seems like if I needed to talk to him, I could just knock on his door and he would answer. He is a fantastic supervisor who supported me through all of the challenges I had in my studies, research, and even in daily life. Being a student and a part of his research team at the BUET Nanocomposite Laboratory in the Department of Materials and Metallurgical Engineering is an honor. Dr. A.K.M. Bazlur Rashid, Professor, and Head of the Department of Materials and Metallurgical Engineering at Bangladesh University of Engineering and Technology (BUET), deserves my deepest gratitude for his insightful advice, academic support, and provision of the tools I needed to complete this research. I want to thank Dr. Fahmida Gulshan, Professor, Department of Materials and Metallurgical Engineering, BUET, and Dr. Ahmed Sharif, Professor, Department of Materials and Metallurgical Engineering, BUET, for their assistance and helpful suggestions. I also want to thank Dr. Muhammad Rakibul Islam, Professor, Department of Physics, BUET, for the scholastic advice, and for giving me access to use his lab facilities. A special word of appreciation goes out to all the faculty in the Department of Materials and Metallurgical Engineering at BUET for your earnest assistance with my thesis project. I would also want to extend a warm thank you to all of the employees in the Department of Materials and Metallurgical Engineering at BUET. I'd also want to express my gratitude to all of my lab mates for their genuine assistance and collaboration. Working with them over the years has been an absolutely amazing experience. I am also grateful to CASR, BUET for providing me the financial support for this research. Finally, I want to thank my parents, my brothers, and the rest of my family from the bottom of my heart for their unwavering support and encouragement during this research project.

Abstract

In this work, a novel MnO_2 nanoparticle incorporated MoS_2 nanoflower (MoS_2/MnO_2) was created using an easy hydrothermal process with varying MnO_2 concentrations(0 wt.%, 2 wt.%, 4 wt.%, and 6 wt.%). For MoS_2 and MoS_2/MnO_2, the Field Emission Scanning Electron Microscope (FE-SEM) images show a three-dimensional flower-like structure. The XRD analysis was used to assess the various structural characteristics of the nanomaterials, which validates the phase purity of MoS_2/MnO_2. The interplanar spacing of the nanostructures changed with the concentration of the MnO_2 nanoparticles, according to Transmission Electron Microscope (TEM) analysis and MoS_2/MnO_2 (6 wt.%) exhibits extended 0.67 nm inter-planar spacing. From the electrochemical investigation, the MoS_2/MnO_2 (6 wt.%) was shown to have a specific capacitance of up to 199.12Fg^{-1} at 0.04 Ag^{-1} current density, high energy density, and exceptional cyclic stability (90% capacitance retention even after 10000 charging/discharging cycles). Due to the produced sample's increased surface area, defect-rich structure, and reduced charge transfer resistance, the specific capacitance of MoS_2/MnO_2 has improved. The creation of effective and affordable energy storage devices will be made possible by the MoS_2/MnO_2 nanostructure, which has enhanced specific capacitance and higher stability.

Table of Contents

List of Figures

List of Tables

List of Abbreviations

NFs	Nanoflowers
NPs	Nanoparticles
TMDs	Transition Metal Dichalcogenides
2D	2 Dimensional
3D	3 Dimensional
EDLS	Electric Double Layer Supercapacitor
FS	Faradaic Supercapacitors
ESR	Equivalent series resistance
TEM	Transmission Electron Microscopy
HR-TEM	High-Resolution Transmission Electron Microscopy
XRD	X-ray Diffraction
SAED	Selected Area Electron Diffraction
2LA(M)	Longitudinal Acoustic Phonon Mode
FESEM	Field Emission Scanning Electron Microscopy
K-M	Kubelka-Munk
CV	Cyclic Voltammetry
GCD	Galvanostatic Charging-Discharging
EIS	Electrochemical Impedance Spectroscopy
CPE	Constant Phase Element

CHAPTER 1

INTRODUCTION

1.1 Introduction

People are becoming more interested in renewable and sustainable forms of energy due to the rapid development of the global economy, increasing consumption of fossil fuels, and the issues with global climate change. Developing solar, wind, tidal, and other renewable clean energy alongside lowering emissions of CO_2 with the improvement of electric automobile is a way to mitigate current energy and environmental pollution problems [1-4]. However, a continuous supply of energy from the renewable sources are not accessible because of the unavailability of sunlight throughout the entire period of time, unreliability of wind and tides together with the unpredictability of nature which possesses a serious drawback to the widespread use of renewable energy sources. A possible way to maintain a sustainable energy future by using energy from renewable clean sources is to use advanced energy storage systems and technologies, such as rechargeable batteries, fuel cells and supercapacitors (SCs) [1,5-7].

Among the available energy storage alternatives, SCs are now in the limelight because most advanced batteries possesses high cost, endurable cycle life, low energy density, etc. makes the batteries unsuitable for applications that requires rapid and higher-power energy in their energy storage systems [12-13]. Supercapacitors are the class of energy storage devices, that can replace the batteries to make rapidly charged energy storage devices to meet the demand of intermediate specific energy [14-15]. Supercapacitors have been attracting much scientific and technical interest owing to their higher power density, safety, advantages of high charge/discharge rate, excellent cycle stability, long cycle life, low temperature operation, low maintenance cost and so on [12,16-18]. Because of these advantages SCs finds its applications as a energy storage tool in diverse field such as public transports, smart door locks, control panels, intercom systems, smart grids, televisions, UPS(uninterruptible power supply) systems, electric vehicle and other electronic devices [19-20]. Furthermore, in heavy-duty applications for example hybrid forklift and cranes, where SCs are able to store energy faster and also can deliver the energy efficiently even in difficult conditions that suggests excellent performance ability of SCs under huge instantaneous power [12].

Active materials play a significant role in designing energy storage devices as the performance of supercapacitors depends on the choice of them. In recent years, Molybdenum disulfide (MoS_2) (transition metal dichalcogenides) has become a popular candidate as the electrode of supercapacitors because of their electrical conductivity , higher surface area , faster intrinsic ion conductivity that suggest exceptional electrochemical properties, etc [21-25]. Molybdenum disulfide (MoS_2), has two-dimensional layered planar structure much like to graphite where the layers are interconnected with sulfur-molybdenum-sulfur bonds and different valence state(+2to+6) of the Mo atoms and also the interlayered space conducive to the electrolytic cation intercalation, give it electrochemically pseudocapacitance property. But MoS_2 shows structural destruction especially aggregation during charge/discharge cycles, no stability of solid−electrolyte interphase (SEI) layer, parasitic reactions related to electrolyte decomposition, poor cycling stability, low energy density, which are the drawbacks for supercapacitors [26-28]. High energy density is one of the most important electrochemical properties of supercapacitor and overall electrochemical property of electrode active material has a significant dependency on its morphology and porosity. MoS_2 nanoflower can give high specific surface area and porosity, where a lot of interfacial active sites are present to react with electrolyte ion [29].

Different metal oxides such as Co_3O_4 ,TiO_2,NiO, V_2O_5,MnO_2 nanoparticles have been added to MoS_2 structure to enhance its capacitive property[30-31]. Liao Xiaobin et al. [32] fabricated MoS_2 nanosheet/MnO_2 nanowire hybrid by lithography technique to analyze the heterogeneous interface impact on the performances of energy storage. Wang et al. [33] have synthesized hierarchical MoS_2/Mn_3O_4 hybrid architectures where Mn_3O_4 nanoparticles are homogeneously incorporated into thin layers of MoS_2 and achieved two times more capacitance than MoS_2 with 69.3% reservation of initial capacitance. Wen et al. [34] have prepared MoS_2 nanowires/$NiCo_2O_4$ nanosheets supercapacitor supported on Ni foam by two step hydrothermal method achieving more capacitance (7.1 Fcm^{-2}) than pure $NiCo_2O_4$ nanosheets. Kanaujiya et al. [29] synthesized mesoporous MnO_2@MoS_2 nanocomposite by using versatile hydrothermal approach. Zhou et al. [35] prepared 1T-MoS_2 nanosheets confined among TiO_2 nanotube arrays for the application of supercapacitor. But, MoS_2 nanosheets preparation methods take time and yield is low and those nanosheets have restacking tendency at the time of charging-discharging that produces high surface energy as a result electrical conductivity reduces [36-40]. To solve those drawbacks, a cost effective with higher yield procedure, for example, simple hydrothermal synthesis route can play

a vital role to produce a flower like stable 3D- MoS_2 nanostructure. Due to have greater surface area alongside with more active sites for electrolytic ion movement, the flower shape nanostructure have the ability to store more energy as well as maintain a longer cycle life when used as the active materials of electrode [41]. Additionally, the incorporation of nanoparticles in the flower shape structure may generate high number of active sites for the diffusion of electrolytic ion, greater stability of the structure and defect rich surface [42]. However Ahmad et al. [43] fabricated Co_3O_4 nanoparticle decorated MoS_2 nanoflower via a facile hydrothermal method where cyclic stability of supercapacitor electrode increases though particle size of Co_3O_4 decreases in the MoS_2/Co_3O_4 nanocomposites. He et al. [44] used hydrothermal method to synthesize MoS_2/MnO_2 nanocomposite to remove Hg^0 in flue gas where growth of MnO_2 on the surface of MoS_2 increases the MoS_2/MnO_2 adsorbent specific surface area. As a result adsorption performance of the adsorbent increases. Sha et al. [45] used template- cum-catalysis free two-step hydrothermal method to create a novel composite composed of alpha-MnO_2 nanorods and hierarchical MoS_2 microspheres for selective and ultra-sensitive detection of nitrite. The sensor's tremendous ability of sensing depends on the heterogeneous interface between constituents of two material, because of the presence of interwined MoS_2 nanosheets of MoS_2 nanoflower and 1D alpha-MnO_2 nanorods, electrical transmission is unobstructed, a significant number of active sites originating from a big number of MoS_2 edges and flaws, a large fraction of metallic (1T) phase in MoS_2 as opposed to semiconducting (2H) phase in MoS_2. Increment of active sites in MoS_2 NF increase the capacitance property of MoS_2 NF [43]. However, as far as we know, the electrochemical behavior of nanocomposites composed of 1D MnO_2 nanorod incorporated MoS_2 nanoflower synthesized with different weight percentage of MoS_2 and MnO_2 has not been studied in detail.

In this study, MoS_2 nano flower/MnO_2 nanorod, a novel structurally combined nanocomposites have been prepared to improve the capacitive performance, power density alongside with higher cycling stability of MoS_2 NF. We have used simple Hydrothermal approach to prepare MoS_2 nanoflower, MnO_2 nanorod and incorporation of rod shaped MnO_2 nanoparticle in MoS_2 nanoflowers in varied concentration(2wt%,4wt%,6wt%). Manganese oxide (MnO_2) is a metal oxide semiconductor and has its own high theoretical capacitance, nontoxic nature, high stability, electro-catalytic activity, lower cost and abundance advantages [46-47]. The addition of MnO_2 nanorod in MoS_2 nanoflower may give more stability in structure, rapid transportation of ion and effective surface interactions with electrolyte ion, as a result capacitance and cycling stability of

MoS_2 Nanoflower may increase [45]. MnO_2 has different polymorphs, among them our synthesized MnO_2 contains double chains of edge-sharing MnO_6 octahedral which exhibits high catalytic activities [48].

1.2 Objectives

The principal objective of this study is to develop hydrothermal synthesis of MnO_2 nanoparticles incorporated three dimensional MoS_2 nanoflowers. The specific aims of the work include:

I. Hydrothermal synthesis of MnO_2 nanoparticles.

II. Incorporation of MnO_2 nanoparticles in hydrothermally synthesized MoS_2 nanoflowers.

III. Investigation and analysis of the structural, morphological and electrochemical properties of the nanoparticles.

1.3 Outline of The Thesis

Chapter 1, give a succinct overview of the problem's current condition, the research's background and purpose.

In **chapter 2**, A summary of the resources utilized in this study will be given. Their synthesis process, key physical features, and literature evaluation in related fields will be discussed. For a better understanding of this research, a brief review of supercapacitors and electrochemical characterizations will be given.

In **chapter 3**, The process for creating MoS_2/MnO_2 nanoparticles will be discussed. The process will be illustrated via a clear diagram. Additionally, the characterization methods and electrode setup for the study of electrochemical properties will be discussed.

In **chapter 4**, Using various characterization procedures, the produced samples' various physical characteristics will be determined, and the examined results will be reported. For a better study, suitable models and computer simulation will be used.

In **chapter 5**, The summary and findings of this study will be reviewed along with potential application areas. Future work possibilities will also be offered.

CHAPTER 2

LITERATURE REVIEW AND THEORETICAL ASPECTS

2.1 Literature Review on MoS_2 Based Energy Storage Electrode

MoS_2 nanosheet/MnO_2 nanowire heterostructure was employed by Liao Xiaobin et al. [32] to make an electrochemical energy storage device. It was possible to create pure MnO_2 nanowires using a hydrothermal process. Spin coating was used to transfer MnO_2 nanowires to the ready silicon wafers, and then Scotch tape was used to stack the layered MoS_2 nanosheets (obtained by micromechanical exfoliation) on top of the MnO_2 nanowires. The MoS_2 nanosheet and MnO_2 nanowire overlap, as shown in SEM photos of the MoS_2/MnO_2 heterostructure displayed in the ESM. At a scan rate of 20 mV/s, the MoS_2/MnO_2 heterostructure can offer a capacity of 0.31 mAh/cm^2. To assess the effect of the heterogeneous interface on the effectiveness of energy storage, two charge/discharge channels were developed. Electrochemical experiments showed a capacity increase of more than 50% when the metal current collector made contact with the MnO_2 side rather than the MoS_2 side. We propose that the unidirectional conductivity of the MoS_2/MnO_2 heterogeneous interface, resulting from unrestricted electrical transport in the MnO_2-MoS_2 channel and the blocking effect on electron transport in the MoS_2-MnO_2 channel, which optimizes reaction kinetics, is responsible for this improvement.

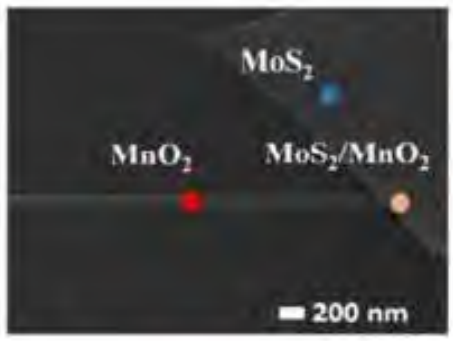

Fig. 2.1 SEM image of the MoS_2 nanosheet (marked with a blue spot), MnO_2 nanowire (red spot), and MoS_2/MnO_2 heterostructure (pink spot) [32].

$MoS_2/Mn3O_4$ hybrid structures as electrodes were produced by Wang et al. [33] using a straightforward and inexpensive hydrothermal and chemical precipitation process based on layered

MoS_2 and Mn_3O_4 nanoparticles. Thin layers of MoS_2 hierarchical structures are homogeneously integrated with Mn_3O_4 nanoparticles. More than two times as much as that of pure layered MoS_2 electrode, the cycle stability of MoS_2/Mn_3O_4 nanostructure still reserves a capacity of 119.3 F/g after 2000 cycles at a current density of 1.0 A/g, or around 69.3% of the original capacitance. The stacked MoS_2 and Mn_3O_4 nanoparticles work together synergistically to provide the positive performance. In order to offer enough active sites for the redox reaction and reduce the distance required for ions and electrons to transfer charge, the layered hybrid exhibits a greater specific surface. While Mn_3O_4 serves as a holder and adds capacity, it also improves the stability of the MoS_2 framework. MoS_2 nanosheets can't re-stack because of the Mn_3O_4 nanoparticles' holding capacity. Additionally, the MoS_2 sheets work as subtractors to raise Mn_3O_4's conductivity. A novel approach to creating high-performance electrochemical supercapacitors is inspired by the layered MoS_2/Mn_3O_4 hybrid.

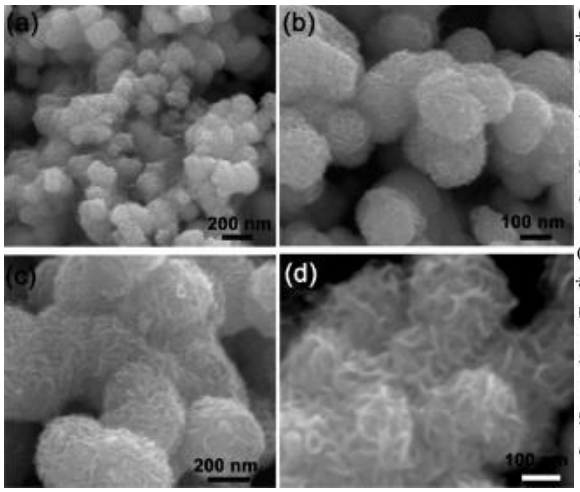

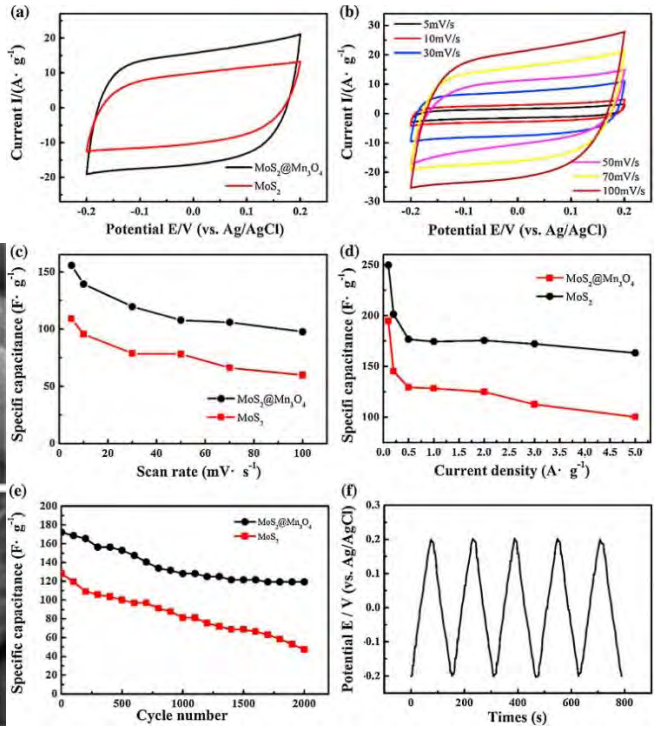

Fig 2.2 SEM image of MoS_2/Mn_3O_4 hybrid [33] **Fig 2.3** (a)CV curve for MoS_2 and MoS_2/Mn_3O_4hybrid at 100mV/s scan rate(b) CV curve MoS_2/Mn_3O_4 hybrid at different scan rate (c)Specific Capacitance vs Scan rate (d)Specific capacitance vs Current density (e) Specific capacitance vs Cycle number (f)Potential vs Time [33].

The flexible hydrothermal technique was used by Kanaujiya et al. [29] to synthesize flower-like MoS_2, spherical MnO_2, and their nanocomposites. X-ray diffraction (XRD), transmission electron microscopy (TEM), and field emission scanning electron microscopy have all been used to conduct structural and morphological analyses on the synthesized materials (FESEM). In order to assess the materials' thermal stability, elemental composition, and functional groups, respectively, Fourier transform infrared spectroscopy (FTIR), X-ray photoelectron spectroscopy (XPS), and thermal gravimetric analysis (TGA) have also been used The Brunauer-Emmett-Teller (BET) study yields surface area and pore size distribution. Using a standard three-electrode setup in 2M KOH aqueous electrolyte at room temperature, the impact of the molar ratio of MnO_2 and MoS_2 on the electrochemical characteristics of MnO_2@MoS_2 nanocomposite has been fully explored. According to the experimental findings, a nanocomposite that was synthesized with a 3:1 molar ratio of MnO_2 and MoS_2 has a higher BET specific surface area (about 133 m^2/g), an ideal pore size distribution, a specific capacitance of 352 Fg^{-1} at 1 Ag^{-1}, a 72% capacity retention rate, and an 88% coulombic efficiency after 2000 cycles at 3 Ag^{-1} in 2M KOH. This sample has a lower relaxation time constant and a greater diffusion coefficient (Da = 3 162.99 x 10^{-10} cm^2 s^{-1}) than other samples. This paper describes and discusses the intricate relationship between electrochemical behavior and structural characterisation of as-made nanocomposites.

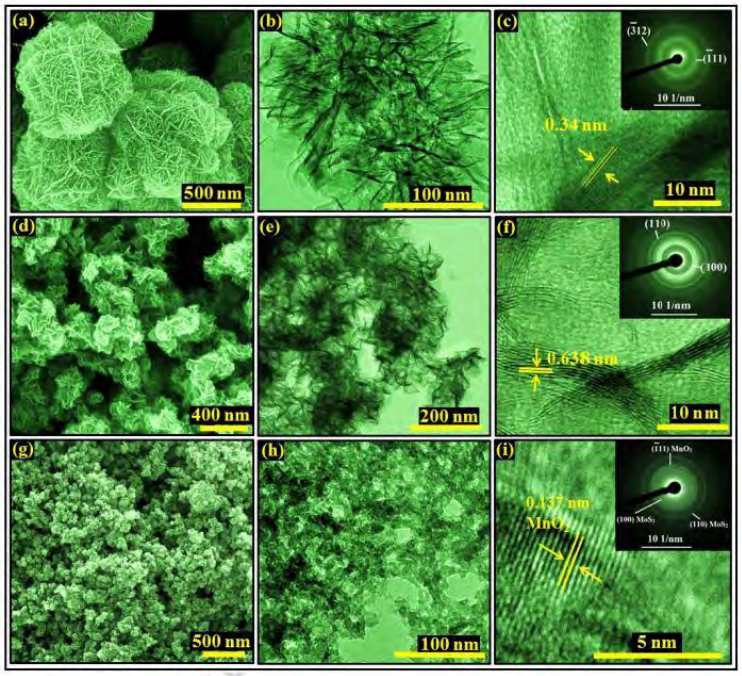

Fig. 2.4 (a)-(c) show the FESEM, TEM and HRTEM images of MnO_2, respectively. (d)-(f) FESEM, TEM and HRTEM images of MoS_2 respectively. (g)-(i) FESEM, TEM and HRTEM images of MnO_2/MoS_2 (3:1)sample, respectively [29].

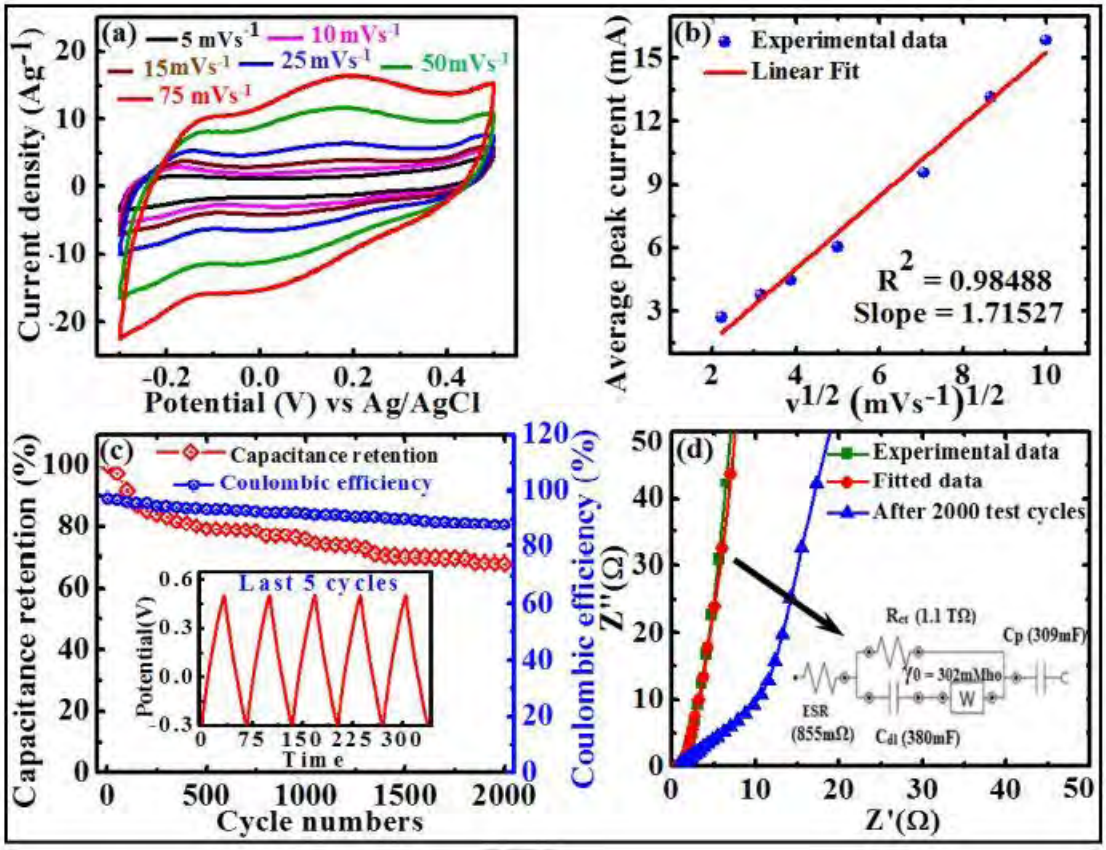

Fig. 2.5 Electrochemical performance of MnO_2/MoS_2 (3:1) composite electrode in 2M KOH aqueous electrolyte: (a) CV curves at the scan rate of 5, 10, 15, 25, 50 and 75 mVs^{-1} , (b) Square root of the scanning rate vs. average peak current, (c) Cyclic stability performance and Coulombic efficiency recorded at 3 Ag^{-1} and inset shows the GCD curve of last 5 successive cycles and (d) Nyquist plots for experimental data, fitted data and after 2000 repeated cycles and inset shows the equivalent circuit diagram [29].

2.2 Molybdenum Disulfide (MoS_2)

One transition metal atom (from the Group IVB, VB, and VIB transition metals) and two chalcogenide atoms (S, Se, or Te) make up the transition metal dichalcogenide most frequently [49]. As seen in Fig. 2.6, these transition metals are covalently bound to two chalcogenide atoms and exhibit +4 oxidation states. Molybdenum disulfide is one of the most extensively studied layered structures among the various transition metal dichalcogenides (TMDs). The S-Mo-S layer is the building block of single-layer MoS_2. Individual single-layer MoS_2 sheets are held together

by weak Van der Waals bonds between two S-S, making bulk MoS_2 an excellent solid lubricant. [50].

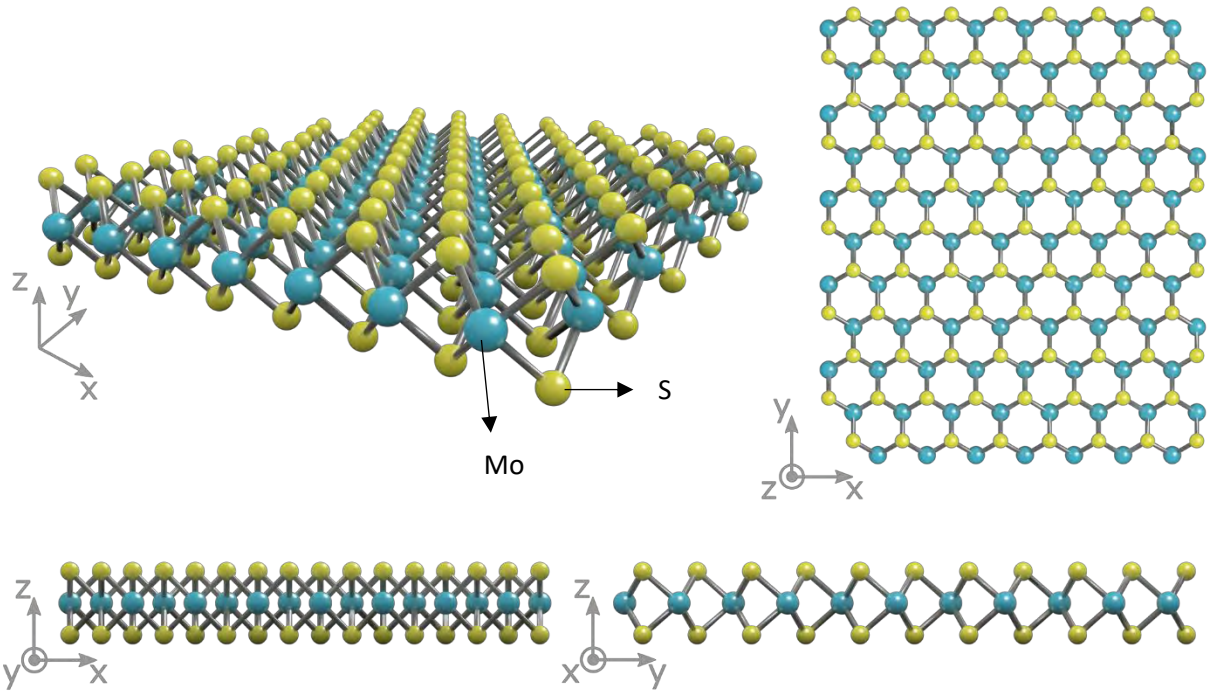

Fig. 2.6 Schematic of layered MoS_2 crystal structure [51].

2.3 Structure of MoS_2

One molybdenum atom is sandwiched between two sulfur atoms in the layered structure of MoS_2, as seen in Fig. 2.6. MoS_2 comes in three primary varieties: 2H MoS_2, 1T MoS_2, and 3R MoS_2. The primary factor influencing these polymorphs is the coordination of metal atoms in the primary unit cell [49,52]. The 2H semiconductor, which is a member of the P63-mmc space group [53]. One MoS_2, in which the coordination of the Mo atom is triangular prismatic, is the most stable phase in this semiconducting structure. As seen in Fig. 2.7(a), the Mo atom is covalently coupled to six sulfur atoms . The intercalation of lithium atoms between 2H MoS_2 layers caused structural distortion in the layers. When seen in Fig. 2.7(b), which belongs to the Space group: P3, the coordination of the Mo atom becomes octahedral as the bottom three sulfur atoms rotate 60 degrees to the upper three sulfur atoms following distortion [52]. MoS_2 is stable, however 1T MoS_2 is metastable and returns to 2H MoS_2 at a gentle annealing temperature of 98°. All six sulfur atoms are visible from the top view of a single layer of 1T phase MoS_2 due to the 60° rotation of the

sulfur atoms, whereas only three sulfur atoms are visible for 2H phase MoS_2 (Fig. 2.7 (a, b)) [54]. High-Resolution Scanning Transmission Electron Microscopy (HRSTEM) [49] may distinguish between the 2H and 1T phases because to the variations in planar densities of these planes, as seen in Fig. 2.7. (c, d)

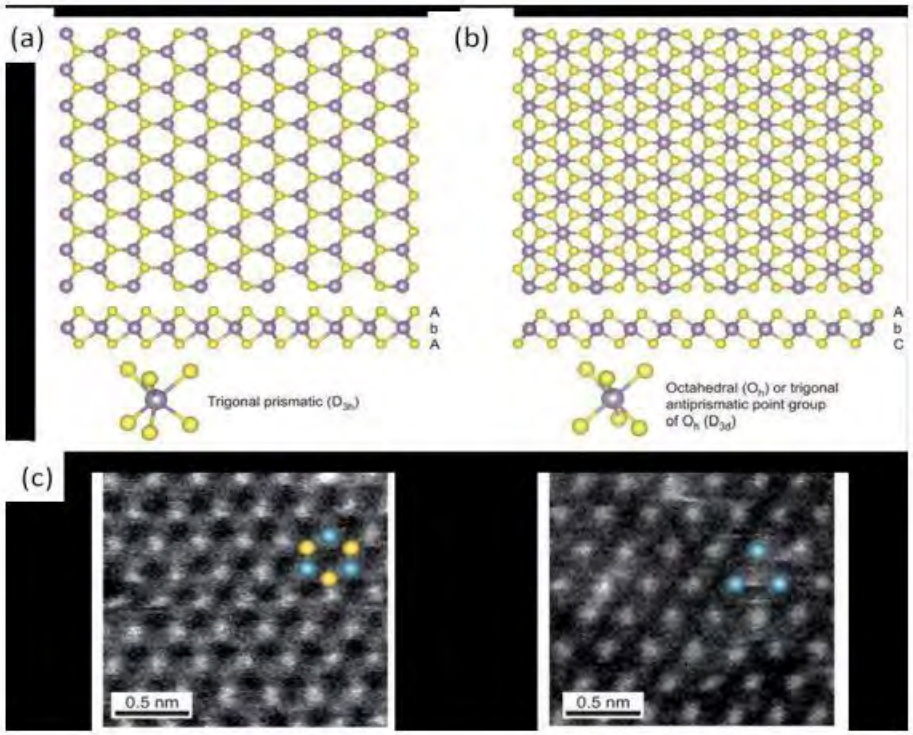

Fig. 2.7 Crystal structure with top view and side view with layer stacking for trigonal 2H phase MoS_2 (a), and octahedral 1T phase MoS_2 (b), Dark-field scanning transmission electron microscopy image of single-layer MoS_2 showing the contrast variation of 2H (c), and 1T MoS_2 (d) [49].

2.5 Structure of Manganese oxide

There are several polymorphic variants of MnO_2 (including α,β, λ, and δ). MnO_2 structures can be divided into chain-like tunnel structures (such as α - and β -type) and the sheet or layered structures (such as δ -type). They differ in that the [MnO_6] octahedra used as their building blocks are connected in various ways; the α-type is made up of double chains of [MnO_6] octahedra that create 2×2 tunnels (Fig 2.10) [55]. Also α -MnO_2 that is constructed from the double chains of edge-sharing MnO_6 octahedra can be linked at the corners to form (2 × 2) + (1 × 1) tunnel structures

(the sizes of the 2 × 2 and 1 × 1 tunnels are 0.46 and 0.189 nm, respectively). The c axis of the tetragonal unit cell is parallel to the direction in which these tunnels expand [56].

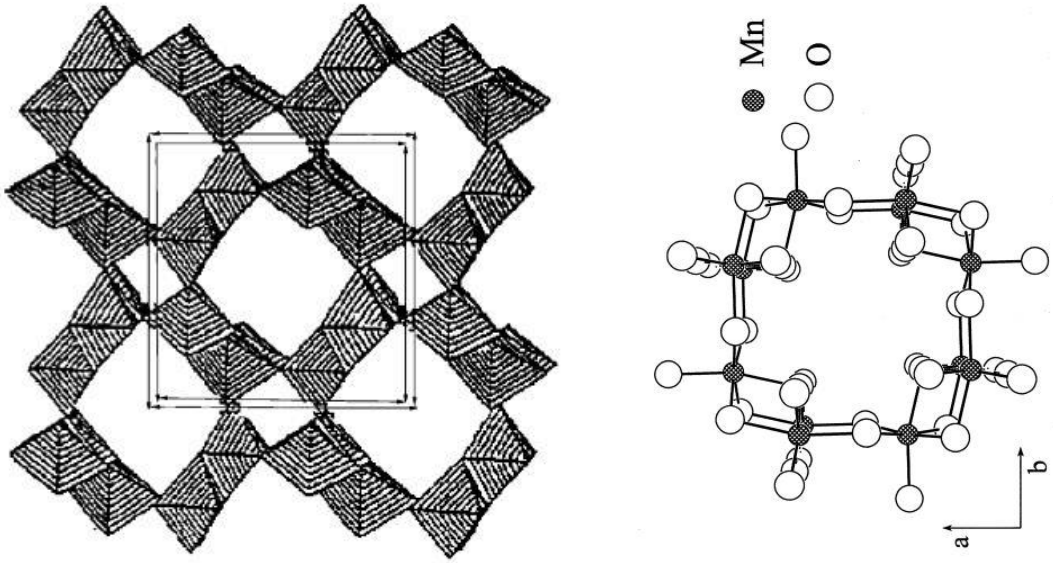

Fig 2.8 The structure of α-MnO_2 [55,56].

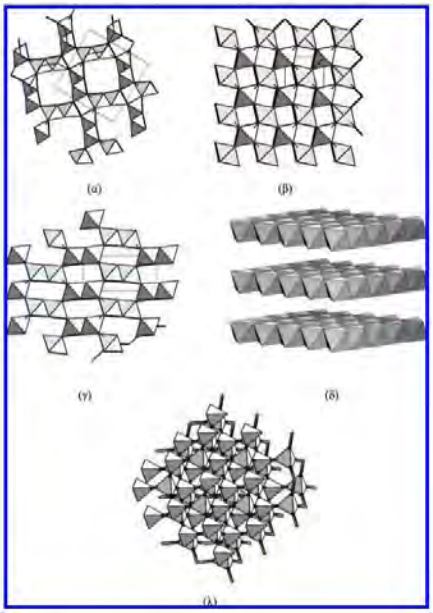

Fig 2.9 Schematic diagram of various crystal structures of MnO_2. a) α-MnO_2, b) β-MnO_2, c) γ-MnO_2, d) ε-MnO_2, e) δ-MnO_2, and f) λ-MnO_2, respectively [57].

2.5 Nanocomposites

Materials that are combined to form nanocomposites have at least one phase with dimensions that fall within the nanoscale range (1 nm = 10^{-9} m). While offering preparatory issues linked to the regulation of elements composition and stoichiometry in the nanocluster phase, nanocomposite materials have emerged as acceptable options to solve the shortcomings of micro composites and monolithic materials. Due to their distinctive design and property combinations that are not present in traditional composites, they are the advanced materials of the twenty-first century. Although the initial conclusion regarding these qualities was published as early as 1992, the widespread comprehension of them has not yet been attained.

2.5.1 Synthesis of MoS_2 and its composites with MnO_2

Many techniques, including mechanical, sonication, electrochemical, chemical, hydrothermal /solvothermal methods of synthesis, and others, can be used to create MoS_2 nanomaterial and MoS_2 based nanocomposite.

2.6 Method of Hydrothermal

By hydrothermal processes, MoS_2 nanomaterial and its nanocomposite with MnO_2 may be created. In general, hydrothermal synthesis is the formation of crystals from chemicals that are insoluble at normal temperatures and pressures (100 °C and 1 atm) under circumstances of high water pressure and temperature. The hydrothermal synthesis is typically conducted below 300 °C since the ionic product has a maximum value of between 250 and 300 °C. 374 °C and 22.1 MPa are the critical water pressure and temperature, respectively. Under supercritical circumstances, the solvent characteristics for many substances, such as the dielectric constant and solubility, alter significantly. At room temperature, when polar inorganic ions may dissolve in water, the dielectric constant of water is 78. With rising temperature and falling pressure, the dielectric constant of water falls. According to the electrostatic theory, the dielectric constant contributes more to reaction rates when it is below 10 under supercritical circumstances. As a result, due to the acceleration of the reaction rate and significant supersaturation, based on the nucleation hypothesis and the decreased solubility, supercritical water provides a suitable reaction media for particle formation.

2.7 Supercapacitor's Principles

The features of supercapacitors are determined by power and energy values, just as in every other energy storage device. Supercapacitors' power and energy may be quantitatively described. The following equation can be used to determine a supercapacitor's maximal energy storage capacity. [58],

$E = 0.5*CU^2$ …….. (2.1)

C is the specific capacitance and U is the maximum cell voltage in Eqn. (2.1). The following equation can be used to determine a supercapacitor P's maximum power. [58],

$P = U^2/(4Rs)$ …..(2.2)

In this equation, U is the maximum cell voltage, and Rs is the corresponding series resistance. As a result, the maximum voltage that can be supplied to the supercapacitor has a significant impact on its energy and power. The equivalent series resistance, which is influenced by the electrode conductivity, electrolyte resistance, contact resistance between the electrodes and the current collector, and ionic resistance of the separator, also has an impact on the maximum power.

2.8 Advantages of Supercapacitors Compared to Batteries

In comparison to batteries, supercapacitors have a number of advantages. They first show a greater power density. Batteries only achieve 150 Wkg^{-1} in terms of power density, but supercapacitors may reach 10 $kWkg^{-1}$. Because they may be charged in a matter of seconds as opposed to batteries' many hours, supercapacitors have greater power densities [59]. With the exception of faradaic supercapacitors, supercapacitors have a longer lifespan than batteries since no faradaic reaction occurs in them. Batteries can endure just 10,000 cycles and have a life expectancy of 5 to 10 years, but supercapacitors may withstand up to 1,000,000 charge and discharge cycles and have an estimated life of 30 years [59,60]. Supercapacitors also have a longer useful life. Batteries will corrode and deteriorate if left unused for a long time. Supercapacitors, on the other hand, will maintain their initial state for years [59]. Supercapacitors achieve an efficiency of around 95% through reversible charge and discharge cycles with little heat loss [59,60]. Additionally, supercapacitors can function in a broad range of temperatures, from -40° C to 70° C. As a result, supercapacitors may be used in a wide range of settings [59]. Supercapacitors are less harmful to

the environment than batteries. They are usually simple to discard and do not contain harmful compounds like lead [59].

2.9 Types of Supercapacitors

According to the method used for storing the charge, supercapacitors may be categorized into two categories. The kind of supercapacitor depends on the electrode materials that are utilized in it.

2.9.1 Faradaic supercapacitors

Faradaic supercapacitors (FS), also known as pseudocapacitors, store energy by quick, reversible redox processes, a method that is similar to that of a lithium-ion battery [61]. Unlike EDLS, the electrode's whole interior and exterior are involved in the charge and discharge processes. Higher capacitance levels and, hence, a more significant increase in energy density are made possible by this. Due to the slower rate of the faradaic redox reactions compared to electrostatic processes, this results in a lower power density than EDLS [62].

2.9.2 Electric double-layer supercapacitor

The materials used in electric double-layer supercapacitors (EDLS) are not electrochemically active, hence the charging and discharging processes are solely physical [63]. The charge may be held on the electrodes thanks to surface dissociation and ion adsorption [64]. Instead of happening across the electrode, this just occurs on the surface. The electrons in the negative electrode travel to the positive electrode when an external electrical charge is introduced. Positive ions migrate from the positive electrode to the negative electrode at the same moment. The electrolyte facilitates this exchange. The process moves quickly and does not degrade the cell because there are no chemical reactions occurring, extending the lifespan of the supercapacitor much beyond that of any other chemical storage device.

2.10 Electrodes

2.10.1 Background

Since the architecture and materials of the electrodes have a significant impact on the electrical characteristics, electrodes are frequently regarded as the most crucial part of supercapacitors. The electrode material employed also determines whether a supercapacitor is an electrochemical double layer or a faradaic device. The capacitance values of supercapacitors are greatly influenced by the electrode's surface area. However, because not all of the surface area is accessible

throughout the charge and discharge operation, the capacitance does not grow linearly with the surface area. Consequently, the area that is directly related to capacitance is described using the phrase "electrochemically accessible surface area" [65]. Cyclic voltammetry is a dependable and frequently used technique for examining and measuring the capacitance behavior of electrodes. Figure 2.10 shows the curves produced on a cyclic voltammetry graph by various electrode materials. An ideal capacitor will plot a perfect rectangular form, but in practice, resistances will cause the shape to change to a parallelogram.

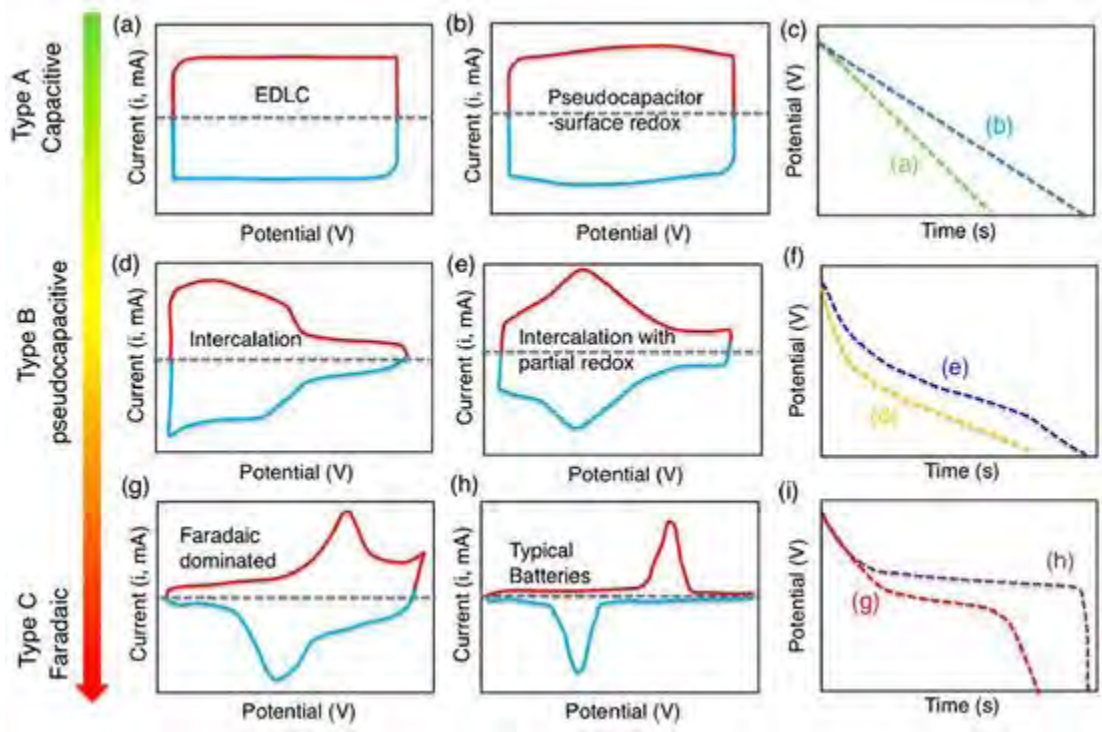

Fig. 2.10 Cyclic Voltammetry diagram of different capacitors [66].

The curve will deviate further from the rectangle and produce peaks in the case of electrodes that experience a faradaic reaction during charge and discharge, such as transition metal oxides and conductive polymers. Higher capacitance values are achieved by faradic materials, however other factors must be taken into account when selecting an electrode material. For instance, the lifespan of faradaic materials is shortened, while ruthenium oxide, which has the highest capacitance value in the chart, is too expensive to be used in any kind of commercial supercapacitor.

2.11 Electrolytes

In the area between the electrodes, electrolytes fill the space and permit the passage of ions. The greatest working voltage of a supercapacitor is dependent on the breakdown voltage of the electrolyte, which is inversely proportional to the supercapacitor's energy and power densities. For this reason, it is a particularly crucial part of the construction of a supercapacitor [67]. The equivalent series resistance (ESR), a factor in determining the power density, is influenced by the electrolyte as well. Wide voltage window, high electrochemical stability, high ionic concentration, low solvated ionic radius, low resistivity, low viscosity, low volatility, low toxicity, low cost, and availability at high purity are all desirable characteristics of an electrolyte [63]. Aqueous electrolytes, organic electrolytes, and ionic liquids are the three categories of electrolytes that are commercially accessible. The solid electrolyte, the fourth type of electrolyte, is uncommon in the sector.

2.11.1 Aqueous electrolytes

Aqueous electrolytes are composed of aqueous solutions of acids. 1 mol L^{-1} H_2SO_4 and 6 mol L^{-1} KOH are the common aqueous electrolytes [68]. Supercapacitors can achieve better conductivity values than their non-aqueous equivalents thanks to aqueous electrolytes. The low voltage window, however, is a major drawback; the thermodynamic window of water exhibits breakdown at only 1.23 V [69].

2.12 Electrochemical Characterization Techniques

The capacity of a material to store charge (Q) per unit electrical potential (V) is known as capacitance (C). Standard electrochemistry methods including cyclic voltammetry, galvanostatic charge-discharge, and electrochemical impedance spectroscopy can be used to determine the stored charge (EIS) [70]. A potentiostat and a frequency analyzer are necessary for these measurements. The analysis setup for the electrochemical cell comes in two different types: (i) two-electrode and (ii) three-electrode configurations [63]. The two-electrode arrangement is utilized for complete supercapacitor devices that have two active electrodes and a separator. Despite not directly revealing the charge contribution from each active electrode, the capacitance measured in such setups reveals the device capacitance. The three-electrode configuration is used to describe each electrode. One active electrode (half-cell) and two extra electrodes, referred to as the reference electrode and counter electrode, are utilized in this design. The system's potential is

fixed using the reference electrode. There are many sorts of reference electrodes depending on the type of electrolyte, such as Hg/HgO for basic solutions and Hg/HgCl for acidic solutions. A counter electrode, such as platinum or graphite, that is chemically inert and electrically conductive is utilized to complete the cell circuit.

2.12.1 CV

A form of potentiodynamic measurement method used to assess the electrochemical behavior of materials is called cyclic voltammetry [70]. This method involves reversibly varying the electrode potential between two potentials while measuring the resulting current. The cyclic voltammogram (CV) is the name of the resulting current-voltage (I-V) curve Figure 2.10 displays typical CV curves for a perfect capacitor and capacitor/resistor. When the potential difference is greater, current grows linearly for resistor materials, and the slope of the curve indicates how much resistance the device has, which is used to determine the material's resistivity. Ideal capacitors, on the other hand, have rectangular CV curves. The infinite resistance of perfect capacitors and the process of charge accumulation under applied DC potential are the foundations for the rectangular curve's nature. When a potential difference is provided to the capacitor, instead of current flowing from one electrode to the next, charges build up on top of each electrode. Due to the device's ability to store charges, the current then initially spikes and saturates. The similar pattern is seen when the potential sweep is reversed. The area in the rectangular curve corresponds to the stored charge in the capacitor.

Stored charge (Q) is proportional to the potential difference (V) between electrodes [70]. where the constant of proportionality is the capacitance (C), as shown in Eqn. (2.3)

$$Q = CV \tag{2.3}$$

By taking the derivative of this equation with respect to time, one obtains

$$\frac{dQ}{dt} = C\frac{dV}{dt} \tag{2.4}$$

where the first expression on the left-hand side of Eqn. (2.4) denotes the so-called changing current I and the last expression denotes scan rate of the potential v, such that

$$I = Cv \tag{2.5}$$

Per Eqn. (2.5), Current is inversely related to the rate at which the potential changes over time (scan rate), and the slope determines capacitance. As can be seen in Fig. 2.10 (a), the typical CV

curves for an ideal capacitor (double layer), a capacitor with finite resistivity, and a pseudocapacitor all deviate from rectangular curves due to internal resistance and ionic diffusion associated to resistance. In addition to the rectangular CV curve shown in Fig. 2.10, any Faradaic reactions also result in a distinct peak; the region inside the CV curve represents the material's capacitance.

2.12.3 GCD

As internal resistance losses are not taken into consideration, capacitance calculations based on CV measurements can occasionally be incorrect. Galvanostatic charge/discharge measurement yields superior results for a capacitance measurement that actually exists. In this method, the electrode is charged at a steady rate, and the change in potential over time is recorded using the reference electrode. Figure 2.11 depicts the triangular galvanostatic charge-discharge curve of an ideal capacitor.

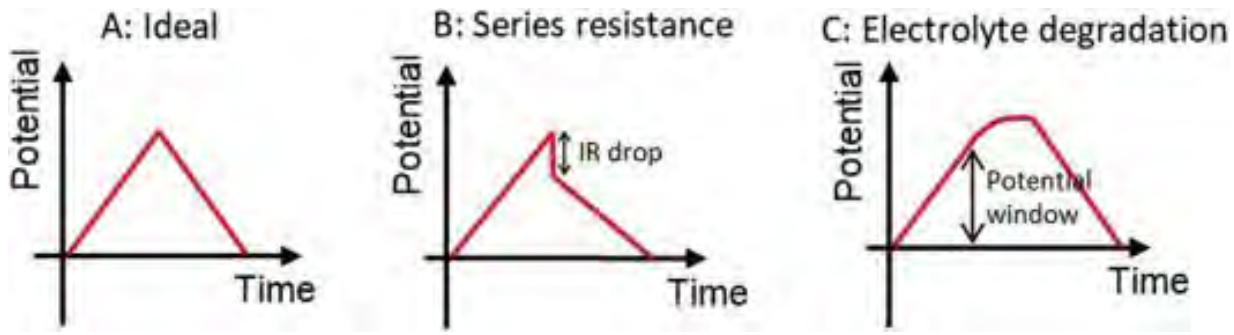

Fig. 2.11 Galvanostatic charge / discharge curve [71].

In actual devices, as seen in Fig. 2.11, the system's internal resistance causes a quick drop in potential during discharging. Low internal resistance is necessary for the ultimate supercapacitor since high internal resistance limits the device's operational potential and shortens the device's discharge time, both of which affect the capacitance of the device. The impact of the internal resistance is crucial since power density and energy density are inversely related to the square of the potential window. Additionally, the internal resistance has an inverse relationship with power density. Low internal resistance is essential for supercapacitor devices with high energy and power densities.

2.12.4 EIS

The capacitive and resistive components of supercapacitor devices can be studied in greater detail using electrochemical impedance spectroscopy (EIS) [72]. The internal resistance of the system is further provided by the galvanostatic charge-discharge approach while the CV technique simply offers the capacitance, making the overall electronic components of a supercapacitor device more complex than just a capacitor and a resistor.As a result, the EIS approach is more useful for learning more about each device component. The diffusion of ionic species in the electrolyte and the porous electrode causes the specific capacitance to shift with the speed of measurement, as was covered in prior chapters. A probe that measures alternating current (AC) is used to account for time. In this section, the term impedance replaces resistance in the I/V relationship and results in

$$Z(\omega) = \frac{v(\omega)}{I(\omega)}; \ \omega = 2\pi f \tag{2.7}$$

$$\Delta V(\omega) = \Delta V_{max} e^{j\omega t} \tag{2.8}$$

Usually, a system's impedance [72] is determined by applying a low-amplitude alternate voltage (V) to a steady potential Vs. Where ω is the angular frequency. This applied potential leads to sinusoidal output current with

$$\Delta I(\omega) = \Delta I_{max} e^{j(\omega t + \varphi)} \tag{2.9}$$

where φ is the phase difference between the current and voltage. Since the impedance is given by

$$z = \frac{\Delta V}{\Delta t} \tag{2.10}$$

Once obtain Z in phasor notation(exponential coordinates) as

$$Z = Z(\omega) e^{-j\varphi} \tag{2.11}$$

which can be expressed as (Using Euler's theorem)

$$Z(\omega) = Z'(\omega) + jZ''(\omega) \tag{2.12}$$

where Z' is a real part of impedance, Z" is the imaginary part of impedance, ω is the angular frequency, and j2 = -1. Nyquist plots can be created to display the frequency response of the supercapacitor electrode by using the real and imaginary components of the impedance as a function of frequency [72]. For an ideal capacitor that is represented by a capacitor and a resistor connected in series, typical Nyquist plots are displayed (Fig. 2.12c), and other combinations of capacitors and resistors (Fig. 2.12d, 2.12e, 2.12f, 2.12g). A diffusion component known as the Warburg term is also introduced for modeling diffusive species in real supercapacitor systems (Fig. 2.13). Equivalent circuit models can be created to characterize and model supercapacitor systems employing these components. Additionally, the double layer capacitances, faradaic capacitances, ohmic resistances, and faradaic resistances with diffusion components (Warburg element) of a quasi-electrochemical system can be calculated using EIS. These AC measurements are usually made between 0.01 Hz and 100 kHz.

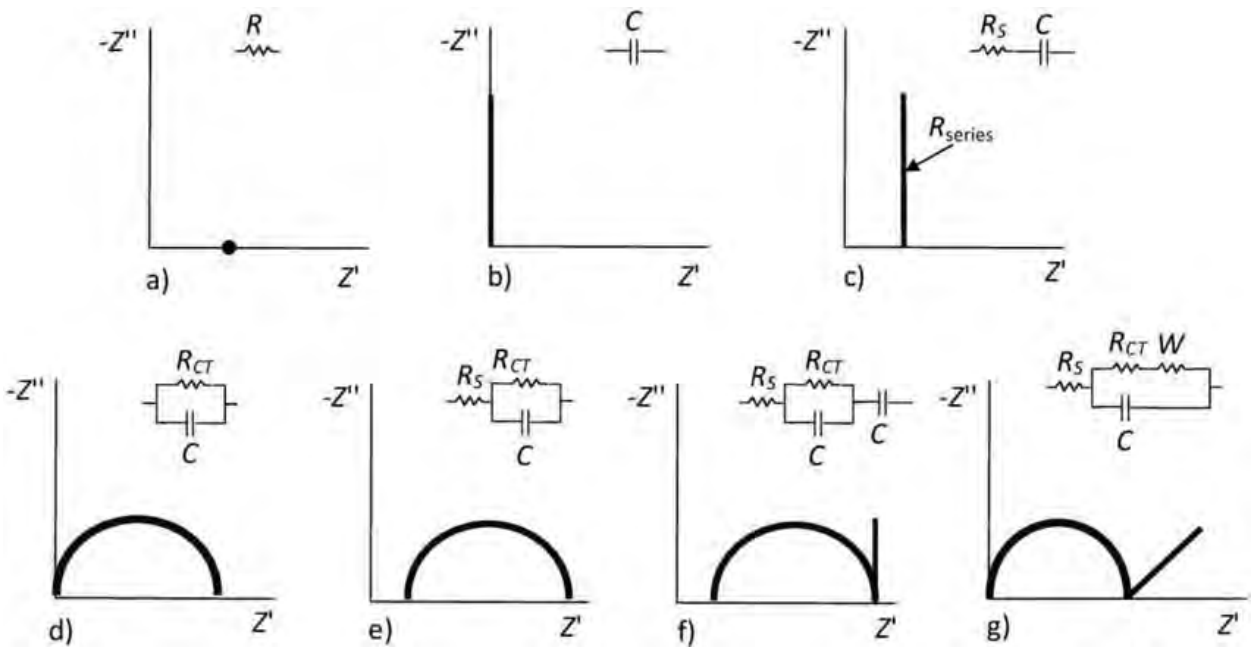

Fig. 2.12 Equivalent circuit models and equivalent Nyquist plot are shown for a capacitor (b), a capacitor and a resistor in series (c), a capacitor and a resistor in parallel (d), and a resistor in series with another resistor and capacitor in parallel (e) [73].

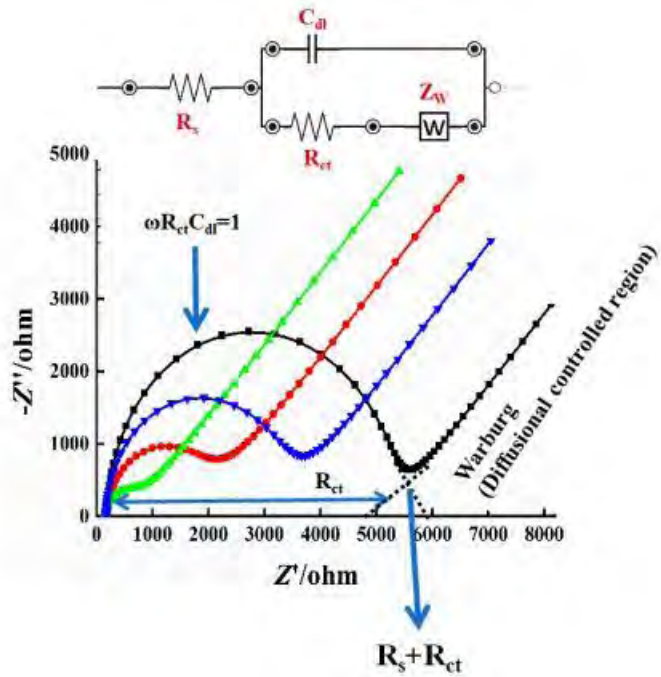

Fig. 2.13 Experimental and simulated impedance spectra showing a simplified Randles equivalent circuit for an electrochemical system [74].

2.13 Electrochemical Setup

An effective method for examining reactions involving electron transfers is electrochemistry. Electrochemistry links changes in chemical composition to electron flow. The ensuing chemical shift in inorganic chemistry frequently involves the oxidation or reduction of a metal complex. An electrode is a material that conducts electricity, usually made of glassy carbon, platinum, gold, or mercury. The voltage can be applied to the electrode to vary the energy of the electrons in the electrode by using an external power source (such a potentiostat). The energy differential between the electrodes is once more the catalyst for this electrochemical reaction. The identification of the molecule utilized as the reductant must be changed in order to alter the driving force of a chemical reduction. The simplicity with which the driving force of a reaction can be regulated and the ease with which thermodynamic and kinetic parameters can be assessed are at the heart of electrochemistry's power. the ease with which kinetic and thermodynamic parameters can be monitored.

Fig. 2.14 Electrochemical Work Station.

2.13.1 Introduction to the electrochemical cell

A brief explanation of the experimental setup used to gather the data is typically provided in the experimental section of articles discussing electrochemical measurements. An electrochemical cell is the container used in a cyclic voltammetry experiment.

2.13.2 Preparation of electrolyte solution

During a CV experiment, electron transfer takes place, and ions in the solution move about to maintain electric neutrality. Ions flow in solution to account for the charge and complete the electrical circuit as electrons migrate from the electrode to the analyte. To aid in lowering the solution resistance, a salt is dissolved in the solvent and is referred to as a supportive electrolyte. The term "electrolyte solution" refers to the combination of the supporting electrolyte and the solvent. Solvent. Increased solution conductivity requires high supporting electrolyte concentrations. The supporting electrolyte will migrate as electron transfers take place at the electrodes to balance the charge and finish the electrical circuit. The concentrations of the dissolved salt have an impact on the solution's conductivity. The solution will be resistive to charge transfer if there isn't enough electrolyte available to achieve charge balance.

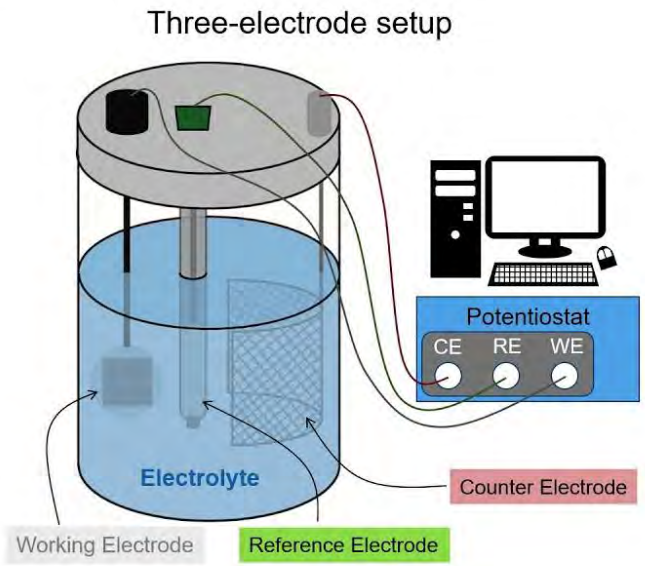

Fig. 2.15 Schematic representation of three electrode system for electrochemical measurements.

2.13.3 Working electrode

The electrochemical event of interest is carried out by the working electrode (WE). The applied potential of the working electrode is controlled by a potentiostat as a function of the potential of the reference electrode. The working electrode's composition of redox inert material in the desired potential range is its most crucial feature. From experiment to experiment, the working electrode can be changed to give various potential windows or to lessen or enhance the surface adsorption of the target species. The working electrode surface must be highly clean and have a well-defined surface area because the electrochemical event of interest happens there. Depending on the type of electrode, different polishing techniques are used, which might also vary from lab to lab. Clean electrode surfaces can be made by mechanical polishing when employing electrodes like glassy carbon or platinum. The electrode is then sonicated in ultrapure water to get rid of the particles. To get rid of any adsorbed species left over after the polishing process, it is frequently also essential to run a number of CV scans in simple electrolytes throughout a large potential window. You can keep doing this until there are no more peaks visible and the scans overlap. Pretreating the electrode is another name for this process. When activated by polishing, the surface of glassy carbon electrodes becomes extremely reactive. When impurities are present in the solvent, they

may choose to preferentially adsorb to the electrode's carbon surface, changing the voltammograms.

2.13.4 Reference electrode

An equilibrium potential for a reference electrode (RE) is clearly defined and constant. It serves as a baseline against which the potential of other electrodes in an electrochemical cell can be measured. As a result, the applied potential is often expressed as "versus" a particular reference. A few frequently used (and typically readily accessible commercial) electrode assemblies feature an electrode potential that is unrelated to the electrolyte that is utilized in the cell. The saturated calomel electrode (SCE), standard hydrogen electrode (SHE), and the AgCl/Ag electrode are a few examples of reference electrodes frequently employed in aquatic media. Typically, a porous frit separates these reference electrodes from the fluid. It is best to match the solvent and electrolyte in the reference compartment to the one used in the experiment in order to reduce junction potentials. Reference electrodes based on the Ag^+/Ag pair are frequently used in non-aqueous liquids. These are composed of a silver wire in an Ag+ salt solution, usually AgNO3. There are conversion tables that allow data collected with an Ag^+/Ag electrode to be compared to data obtained with other types of reference electrodes for a variety of silver salts, solvents, and concentration combinations. Due to variations in [Ag+], electrolyte, or solvent utilized, the potential of Ag^+/Ag reference electrodes can change from experiment to experiment, thus it's crucial to pay attention to the particulars of a non-aqueous reference electrode. Reduction potentials should be compared to an internal reference drug with a known E0′ in order to get around these issues. Researchers are recommended to use reported potentials against the ferrocene couple at 0 V versus Fc^+/Fc as a reference since ferrocene is frequently used as an internal standard in all experiments. The potential window of the analyte's redox processes should be carefully checked to make sure that it does not overlap with those of ferrocene and that the analyte does not interact with ferrocene. If so, alternative internal standards with clearly defined redox couples, such as decamethyl ferrocene, may be utilized. We suggest including ferrocene in all measurements rather than adding it at the conclusion of a data set since non-aqueous reference electrode potentials have a tendency to vary throughout the course of an experiment.

2.13.5 Counter electrode

The current starts to flow when a voltage is given to the working electrode that allows for the reduction (or oxidation) of the analyte to happen. The counter electrode's (CE) job is to finish the electrical circuit. As electrons move between the WE and CE, current is recorded. The surface area of the counter electrode is higher than the surface area of the working electrode to make sure that the kinetics of the reaction occurring at the counter electrode does not hinder those occurring at the working electrode. The counter electrode is commonly a platinum wire or disk, although there are other counter electrodes made of carbon. Oxidation takes place at the CE when looking at a reduction at the WE. Therefore, it is important to choose a CE that is as inert as feasible. Depending on the experiment, counter electrodes may occasionally be separated from the rest of the system by a fritted compartment since they may produce byproducts. When researching a reductive process in THF at the WE, one example is the oxidative polymerization of THF that can take place at the CE.

CHAPTER 3

MATERIALS SYNTHESIS AND CHARACTERIZATION TECHNIQUES

This chapter provides a brief explanation of the hydrothermal procedure, which was employed to manufacture the target material for this thesis. Additionally, several characterization methods used to examine the produced nanomaterials are addressed in this article.

3.1 Materials

Without further purification analytical pure grade chemical reagents were used in this study. Sodium molybdate dihydrate ($Na_2MoO_4 \cdot 2H_2O$), Potassium permanganate ($KMnO_4$), Manganese sulphate monohydrate ($MnSO_4.H_2O$) and Dimethyl sulfoxide (C_2H_6OS) were obtained from Merck, Darmstadt, Germany. Thiourea (CH_4N_2S), Polyvinyl alcohol (PVA) $(C_2H_4O)_x$ and Sodium sulfate (Na_2SO_4) were obtained from Research Lab, India.

3.2 Preparation of MoS_2 NF

0.14M Sodium molybdate dihydrate ($Na_2MoO_4 \cdot 2H_2O$) and 0.65M thiourea (CH_4N_2S) were dissolved in 120 ml deionised water followed by vigorous stirring to form a clear precursor solution, which was transferred into a 250 ml Teflon-lined autoclave. The autoclave was then heated in an electric oven at 200°C for 24 h. After the autoclave was cooled down naturally to room temperature, black precipitate was harvested by centrifugation and washed several times with deionized water and ethanol. To get MoS_2 nanoflower the resultant black powder was dried in an electric oven at 60°C for several hours.

3.3 Preparation of MnO_2 nanorod

A 5.6878g portion of $MnSO_4.H_2O$ was dissolved in 140 mL of deionized water, and then 2.3657 g $KMnO_4$ particles were added into the solution with stirring. After stirring for 30 minutes the suspended solutions were subsequently transferred into a Teflon-lined stainless steel autoclave with a volume of about 250 mL, sealed and maintained at 140° for 12 h in an electric oven. After the autoclave was cooled down naturally to room temperature, brown precipitate was centrifuged and washed several times with deionized water and ethanol. To get MnO_2 nanorod the resultant brown powder was dried in an electric oven at 80°C for several hours.

3.4 Preparation of MnO_2 incorporated MoS_2NF

At first desired amount of MnO_2 nanorod was taken into 50 ml deionised water and sonicated for 1 hour to prepare 2 wt.% MnO_2 incorporated MoS_2NF. By dissolving 0.14M Sodium molybdate dihydrate ($Na_2MoO_4 \cdot 2H_2O$) and 0.65M thiourea (CH_4N_2S) in 70 ml deionised water followed by vigorous stirring, and then transferred the solution into the sonicated 50 ml MnO_2 solution followed by vigorous stirring for 1 hour. Then the suspended solution was transferred into a Teflon-lined stainless steel autoclave, sealed and maintained at 200°C for 24 h in an electric oven. As desired black precipitate was centrifuged and washed several times with deionised water and ethanol. To get the MoS_2/MnO_2(2wt%) nanocomposite the resultant powder was dried at 80°C for several hours. Various amount of MnO_2 nanorod such as 2, 4, and 6 wt.% was used and the resulting nanocomposite materials are entitled as MoS_2/MnO_2 (2wt%), MoS_2/MnO_2 (4wt%) and MoS_2/MnO_2 (6wt%) respectively.

3.5 Preparation of electrode

To make working electrodes a slurry of active material was deposited on a cross sectional surface ($0.3cm^2$) of a glassy carbon electrode. The slurry was prepared by mixing the active material with PVA (4% of active material) and Dimethyl sulfoxide and sonicated the whole mixtures for 1 hr. After depositing the slurry the working electrodes were dried at 65°C for several hours. Here PVA acts as a binder because the hydroxyl groups it possess can make well bonded hydrogen bonds with both the glassy carbon electrode and active materials [75-76]. Dimethyl sulfoxide is a polar aprotic solvent that dissolves both polar and non-polar compounds so as a solvent it was used.

3.6. Characterizations

3.6.1 Field emission scanning electron microscope

To get the microscopic information about the surface of synthesized samples field emission scanning electron microscopy (FE-SEM) (JSM 7600, Jeol) image was taken. The composites were coated with a thin gold/palladium layer prior to imaging.

3.6.2 Transmission electron microscope

The microstructure and morphology of the synthesized samples were also observed by high resolution transmission electron microscopy (TEM) (JEOL, JEM 2100 F). A small quantity of the materials were sonicated for 20 minutes in 2 mL of ethanol to prepare the TEM sample. The

sonicated sample was then dropped onto a 3 mm carbon-coated Cu grid. The sample was placed under the microscope after being allowed to dry.

3.6.3 X-ray diffraction

By using the radiation of CuK_{α} (λ = 1.5406 Å) of X-ray diffractometer (3040XPert PRO, Philips), got the XRD data.

3.6.4 Electrochemical measurement

The electrochemical performances of the electrodes composed of bare MoS_2 NF and different percentages of MnO_2 incorporated MoS_2 NF were studied by using a CS310 electrochemical workstation (corrtest, china) in 0.5 M Na_2SO_4 electrolyte using a three electrodes system.

Here working electrode: glassy carbon electrode,

reference electrode: Ag/AgCl,

counter electrode: platinum plate (1 cm × 1 cm).

CHAPTER 4

RESULTS AND DISCUSSION

4.1 Scanning electron microscopy

FESEM image of MnO_2 (Fig. 4.1(a)) shows densely aligned nanorod shape structure which are disorderly arranged with the length of several micrometer and width in the range of 47-98 nm. In high magnification (Fig. 4.1(b)) the surface of the bundled nanorods appears smooth [45,77].

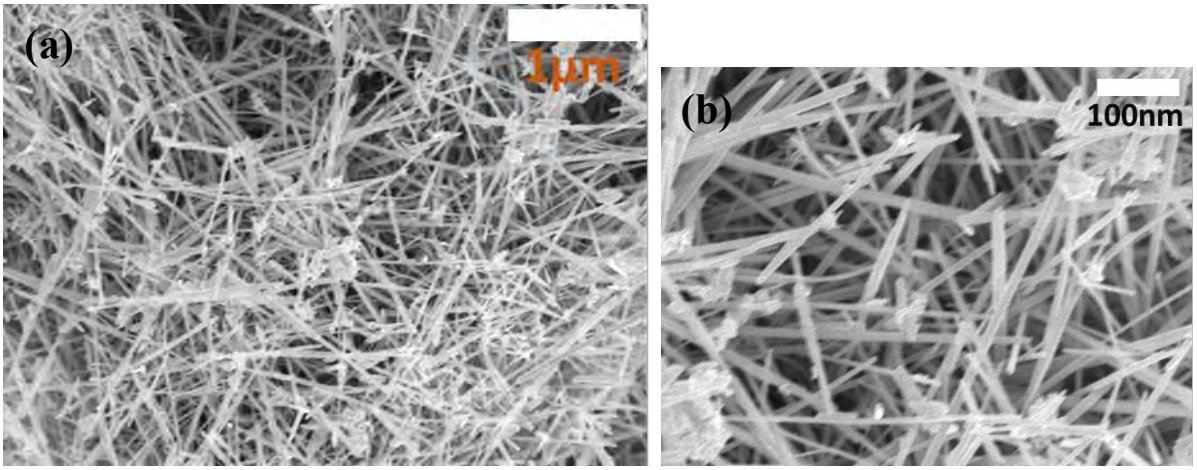

Fig. 4.1 FE-SEM image of MnO_2 nanorod at (a)low magnification, (b)high magnification.

From FESEM image of MoS_2 (Fig. 4.2(a)), flower-like spherical 3D nanostructure confirms successful synthesis of MoS_2 nanoflower with diameter of 5-6μm. Those nanoflowers consist of plenty of aligned curved petals, which are assembled by several MoS_2 nanosheets, through a common inner center. The petal thickness is observed in the range of 20-50nm by using ImageJ software [78].

Fig. 4.2(b-d) shows the FESEM images of MoS_2/MnO_2 nanocomposite where the curved petals of MoS_2 are more uniform and smoothly aligned which proves MnO_2 nanorod acted as a backbone. These nanoflowers with observed diameter in the range of 4−6μm are cluster form or not dependent to each other [79]. When MnO_2 nanorod was immersed into the MoS_2 precursor solution , the Mo^{4+} ions from cationic precursor could be attracted on the surface of MnO_2 nanorod because of van der Waals, cohesive or electrostatic or other chemical forces [45]. S^{2-}ion from anionic

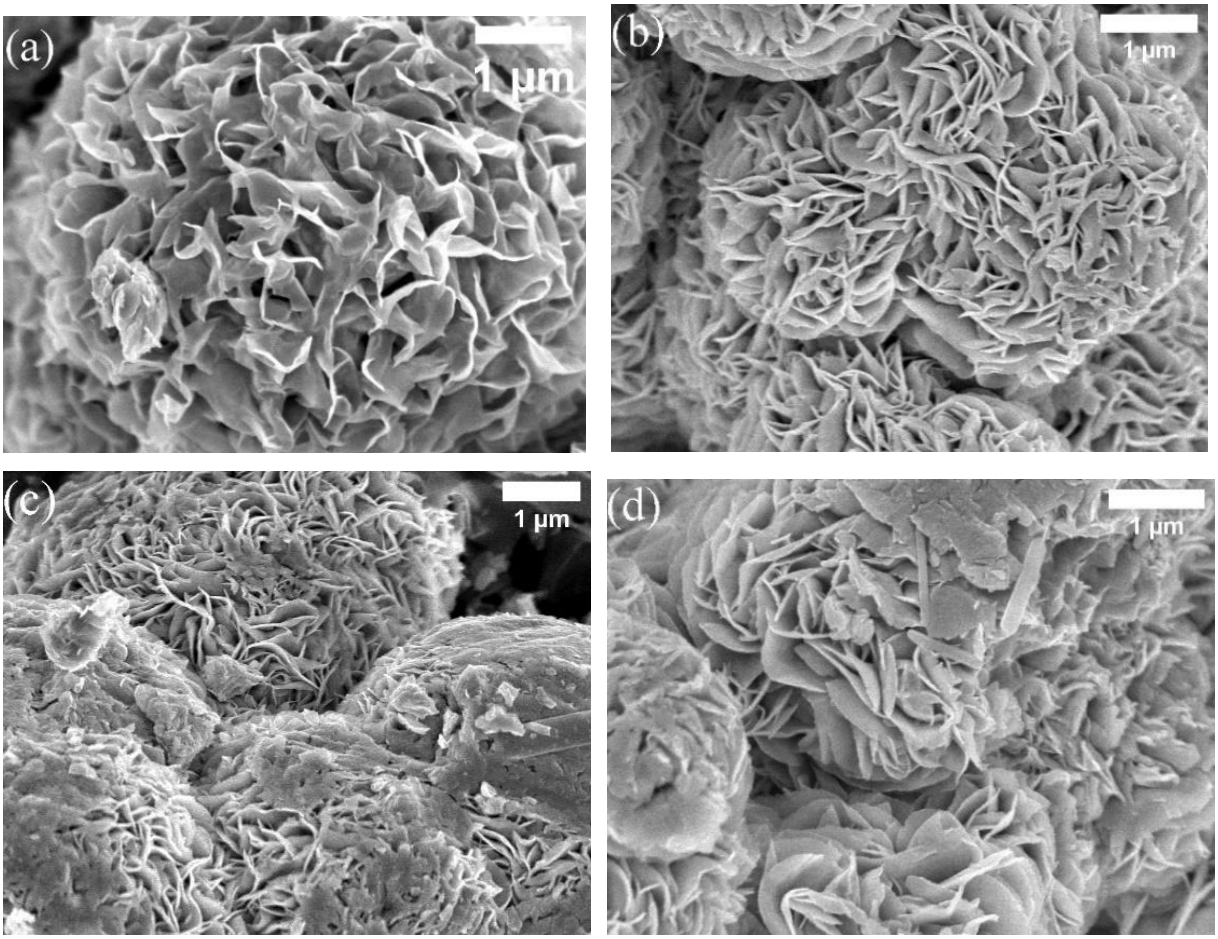

Fig. 4.2 FE-SEM image of (a) MoS_2 nanoflower, (b) MoS_2/MnO_2 (2wt%), (c)MoS_2/MnO_2(4wt%), and (d)MoS_2/MnO_2(6wt%) nanocomposites.

precursor combine with Mo^{4+} ions on the surface of MnO_2 nanorod form flower shape nanostructure. From Fig. 4.2(b-d) we observe that the diameter of the MoS_2 nanoflower gradually decreases as the concentration of MnO_2 addition increases and the thickness of petal for MoS_2/MnO_2(2wt%) is in the range of 10-20 nm but for MoS_2/MnO_2(4wt%) and MoS_2/MnO_2(6wt%) the thickness (20-40nm) of petal increases because of the agglomeration of multiple layers of nanosheets [80,81]. Due to increase of petal thickness, porosity and specific surface area would increase as a result more electrical contact with current collector provide excellent charge transfer rate and improvement in electrochemical capacity. In Fig. 4.2(b-c) existence of MnO_2 nanorods are not clearly observed due to low concentration of MnO_2 but agglomeration of the MoS_2 NF and presence of dispersed foreign particle on the surface of the petals with elemental distribution of Mo, S, Mn, O from EDX mapping shown in Fig. 4.3(b-d)

confirms the petals consist of Mo and S and the foreign particle has Mn and O. When the concentration of MnO_2 increases,

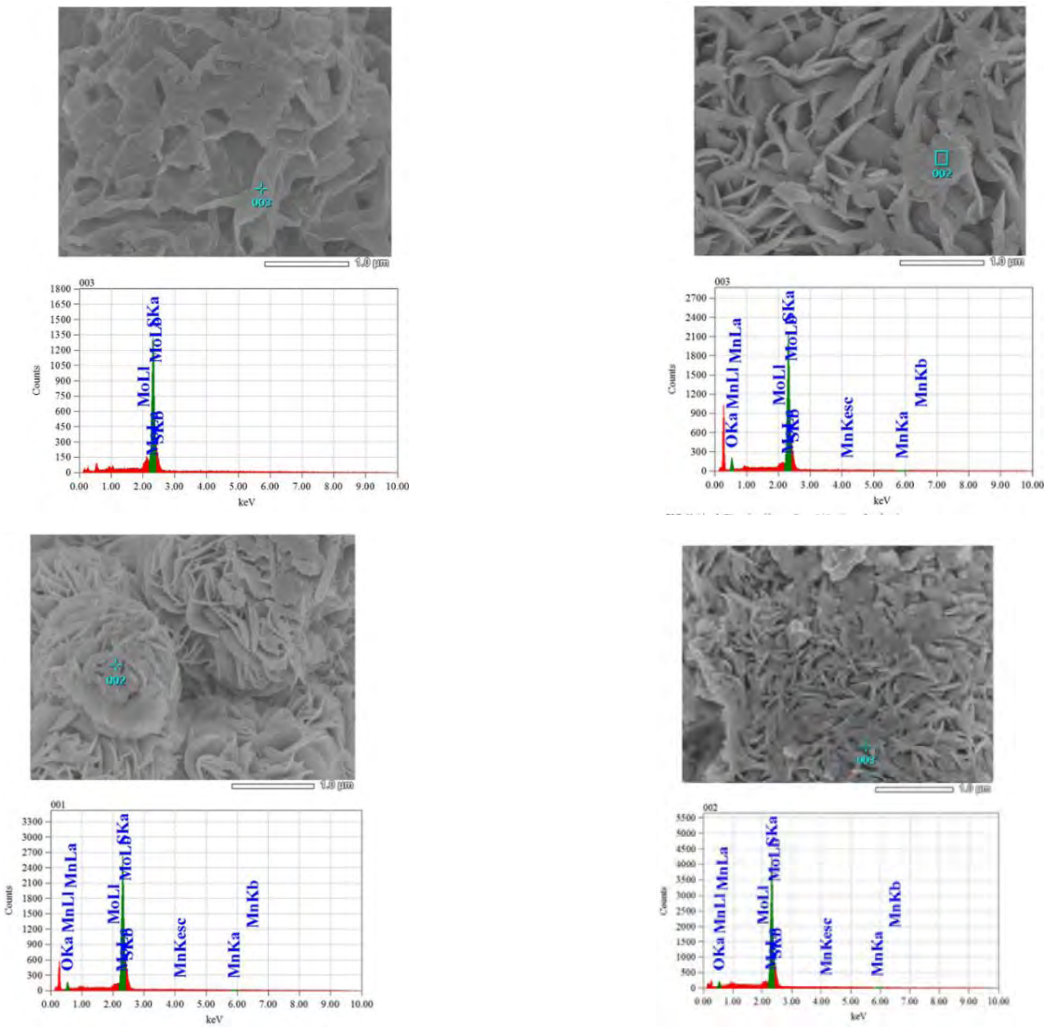

Fig. 4.3 EDX spectra of (a) MoS_2 nanoflower, (b) MoS_2/MnO_2 (2wt%), (c) MoS_2/MnO_2 (4wt%), and (d)MoS_2/MnO_2 (6wt%) nanocomposites.

nanorods are clearly observed in Fig. 4.2(d)where breaking of some nanoflower is observed. So,Combination of 3D nanoflower and 1D nanorod may provide structural stability which may give excellent cycling stability and superior rate performance.

4.2 Transmission electron microscopy

Fig. 4.4(a–d) and Fig. 4.5(a-d) show the TEM images of MoS_2 NF and MoS_2/MnO_2 nanocomposite and HR-TEM image along with the corresponding SAED (selected area electron diffraction) patterns, respectively. Fig. 4.4(a) shows TEM image of MoS_2 NF that consist of many thin petals

and those petals are composed of several MoS_2 nanosheets. From HRTEM image, in Fig. 4.5(a), we observed disorderly arranged lattice fringes and weak diffraction rings in the inset SAED pattern confirms poor crystallinity of MoS_2 NF [82]. The poor crystalline nature is also verified by weak and broad diffraction peaks in the XRD pattern (Fig. 4.7) [83]. The magnified HRTEM image (Fig. 4.5(a)) shows the interlayer spacing is 0.63 nm, which agrees well with the (002) plane.

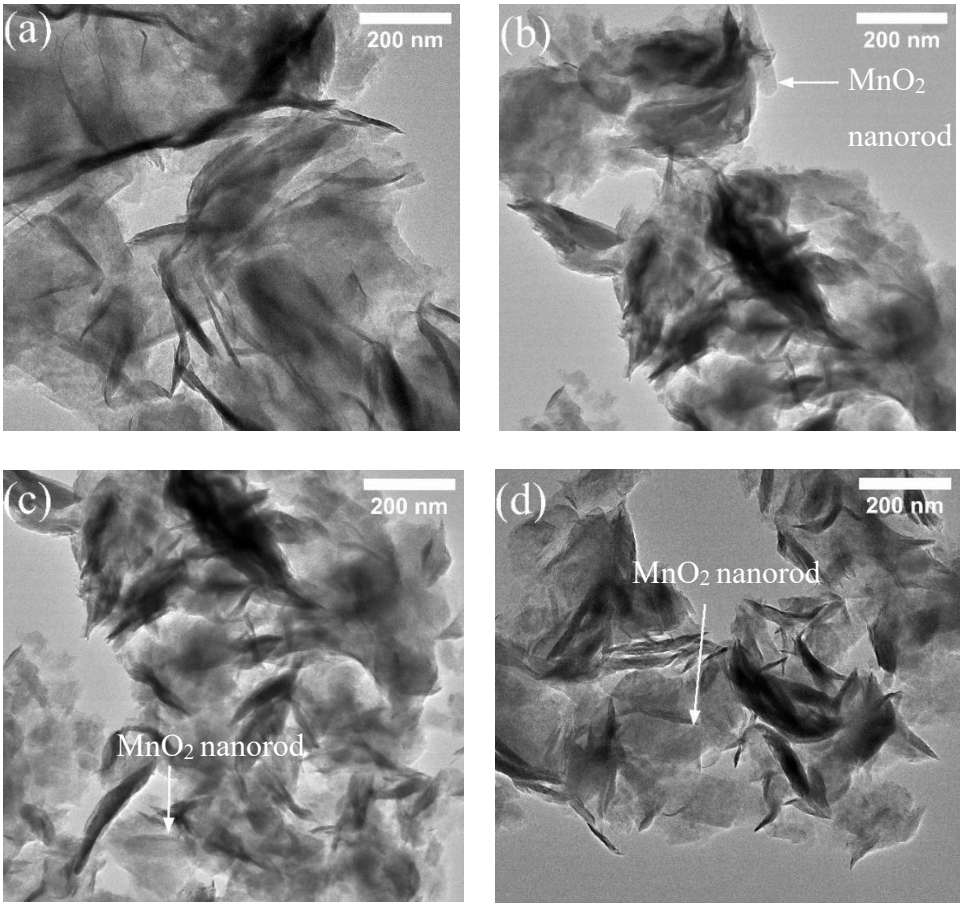

Fig. 4.4 TEM image of (a) MoS_2 nanoflower, (b) MoS_2/MnO_2 (2wt%) ,(c) MoS_2/MnO_2 (4wt%) ,and (d)MoS_2/MnO_2 (6wt%) nanocomposites.

MoS_2 which indicates hexagonal nanosheets grow along the vertical [0 0 2] crystal axis [84]. Fig. 4.4(b-d) is the TEM image of the MoS_2/MnO_2 nanocomposite, shows the curved and wrinkled nanosheets of MoS_2 are very thin and partially transparent. Light contrasts in various areas indicate ultrathin nature of the nanosheets. The SAED pattern of the composite (inset Fig. 4.5), consists of five clear rings, four of which correspond to (100), (103), (105) and (110) lattice planes of MoS_2

and the remaining one is indexed with (521) lattice plane of MnO_2.Inset Fig. 4.5(a) shows the lattice planes of MoS_2 and (400), (411), (541) and (600) planes of MnO_2 nanorod. These results confirm the successful synthesis of MoS_2/MnO_2 nanocomposite and intimate contact between MnO_2 nanorod and MoS_2 NF. In addition, XRD pattern has good agreement with the crystal faces, also supporting the Tetragonal and hexagonal structure of MnO_2 and MoS_2, respectively.

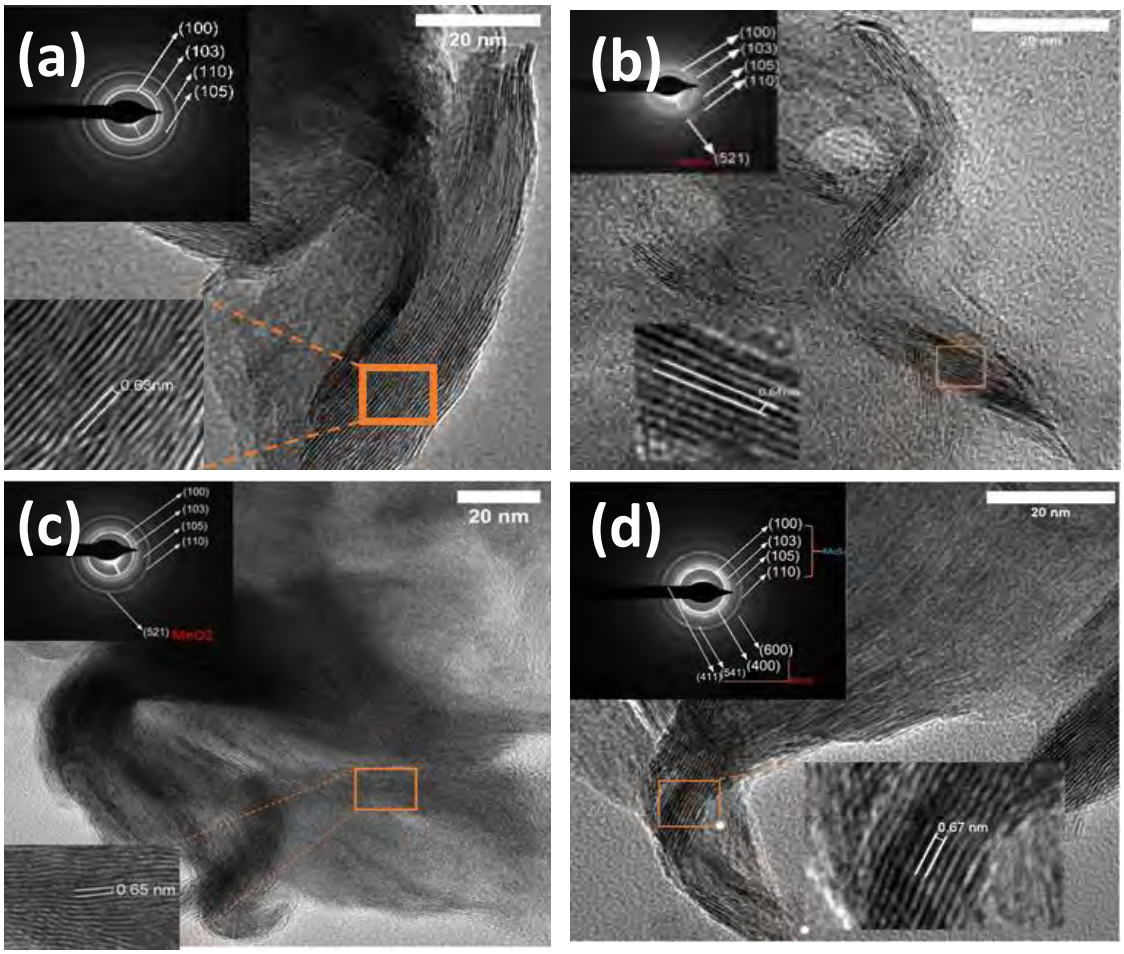

Fig. 4.5 HR-TEM image of (a) MoS_2 nanoflower, (b) MoS_2/MnO_2 (2wt%), (c) MoS_2/MnO_2 (4wt%) , and (d)MoS_2/MnO_2 (6wt%) nanocomposites. Inset of 4.5(a–d) shows the corresponding SAED pattern.

From the TEM images of nanocomposite, discontinuity in the lattice fringes of the curled edges, suggests the presence of excess dislocations and defects in the crystals [79,85]. The inset SAED pattern (Fig. 4.5(b-d)) shows few bright concentric diffraction rings that ensures polycrystalline nature of the nanocomposite due to the coexistence of MoS_2 and MnO_2 .In the TEM image(Fig.

4.4(d)) of MoS_2/MnO_2(6wt%) nanocomposite, the presence of MnO_2 nanorod between MoS_2 nanosheets is clearly visible. Transfer of electrons between MoS_2 and MnO_2 is facilitated due to close integration between MnO_2 and MoS_2. The interlayer spacing increases to 0.64nm, 0.65nm and 0.67nm in MoS_2/MnO_2(2wt%), MoS_2/MnO_2(4wt%) and MoS_2/MnO_2(6wt%) samples, respectively, indicating a significant lattice expansion [28]. The gradual increase of interlayer spacing with the increase of MnO_2 concentration may be due to the diffusion of Mn^{4+} and O^{2-} ions between MoS_2 layers. The enlargement of interlayer spacing and unique nanoflower-nanorod morphology provides better ions intercalation, more electroactive sites and enhancement of electrolyte access that gives desire electrochemical property with improve efficiency in attaining higher capacitance [29,45,86].

4.3 X-ray diffraction

The X-ray powder diffraction (XRD) patterns were studied to confirm the structure, phase and crystallinity of MnO_2 nanorod, MoS_2 nanoflower, and MoS_2/MnO_2 nanocomposites, as shown in Fig. 4.6 and Fig.4.7. It can be seen from Fig. 4.7 that the diffraction peaks of the pristine MoS_2 can agree well with the hexagonal MoS_2 phase (JCPDS No. 37-1492) which belongs to the space group P63/mmc. The peaks at 2θ= 14.04°, 33.49°, 39.46°, 48.57° and 59.14° are attributed to the (0 0 2), (1 0 0), (1 0 2), (1 0 3), (1 05) and (110) planes, respectively [79]. All the reflections of the XRD pattern in Fig.4.6 can be readily indexed to a pure tetragonal phase [space group: I4/m (no. 87)] with lattice constants of a = 0.985 nm and c = 0.285 nm. No peaks for other types of manganese oxides are observed, indicating that the as-prepared products are phase-pure MnO_2 nanorods [87].

In Fig. 4.7(a) The intense peak of pure MoS_2 nanoflower at 14.04° corresponds to the (002) plane with a d-spacing of 0.63 nm, indicating that layered MoS_2 grows well stacked along the c axis during synthesis [88]. Compared with the pure MoS_2nanoflower, the diffraction peaks of MoS_2/MnO_2 nanocomposites in Fig. 4.7 can also be assigned to the hexagonal MoS_2 phase.

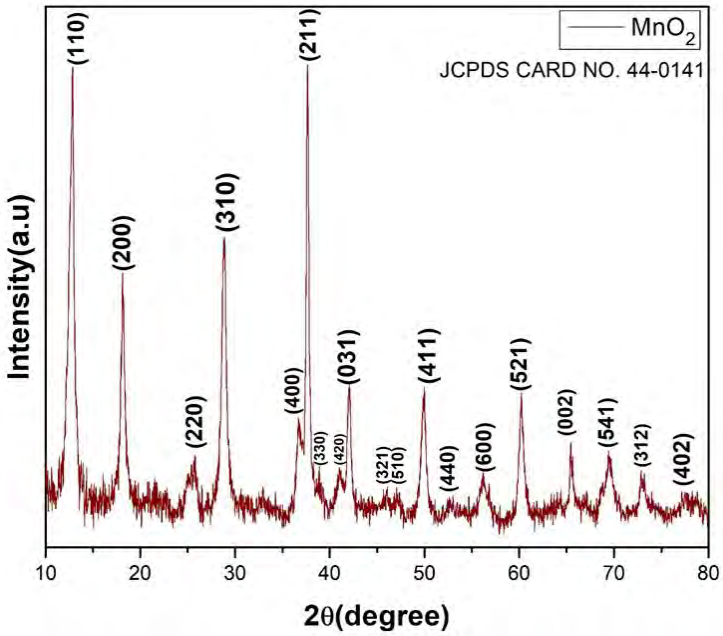

Fig 4.6 XRD pattern of as prepared MnO_2 Nanorod.

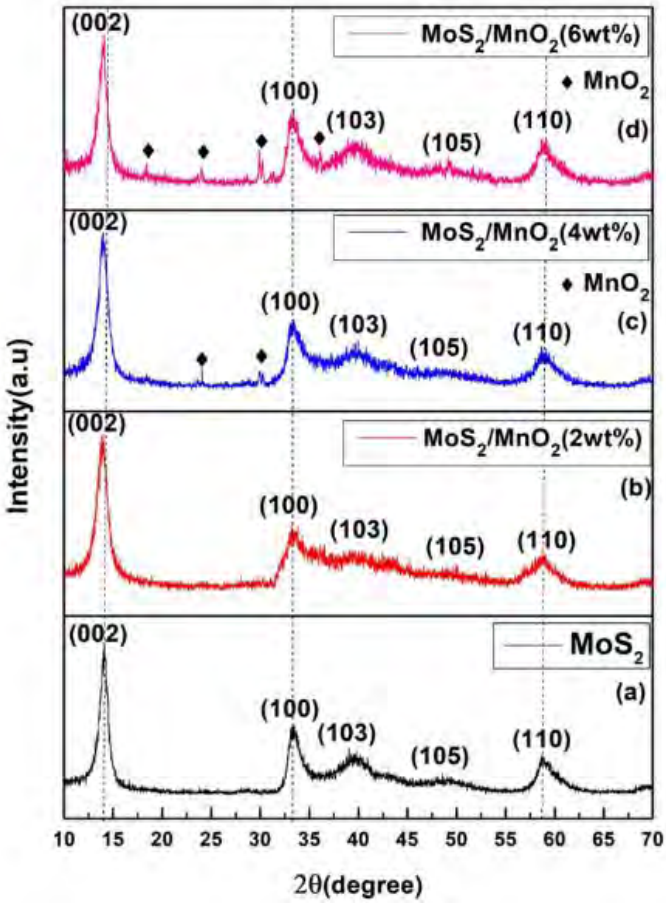

Fig. 4.7 XRD pattern of Pristine MoS_2 nanoflower and as prepared MoS_2/MnO_2 nanocomposites.

For MoS_2/MnO_2 nanocomposites, every main characteristic peak of pure MoS_2 can be observe in every type, but in contrast, the main characteristic peaks of MnO_2 can be only observed clearly in the Fig. 4.7(c) and Fig. 4.7(d) MoS_2/MnO_2(4wt%) and MoS_2/MnO_2(6wt%) nanocomposites, which can be explained by the difference in crystallinity between MoS_2 andMnO_2, as well as because of the smaller amount of MnO_2 in the MoS_2/MnO_2 nanocomposites [89]. It is obvious that the peak of MnO_2 strengthened due to the proportion of MnO_2 increases. It is worth noting that the peak position of pure MnO_2 is at lower θ than that of the composite. The reason may be that the second hydrothermal preparation optimized the crystallinity of MnO_2 [90,44]. In Fig. 4.7(b-d) the broadened and weak diffraction of (002) plane implies the low crystallinity, suggesting that the mean crystallite size of the MoS_2/MnO_2 is much smaller than that of the pristine MoS_2 and also indicating the petal of MoS_2 nanoflowers constituted by a few layers of nanosheets [83]. Shifting the first XRD peak to a lower angle indicates an expansion of interlayer distance in MoS_2.Besides, the slight (002) peak shift compared with standard hexagonal phase MoS_2 is ascribed to the lattice distortion for the synthesized MoS_2 nanoflowers [83,91].

The crystallite size (L), dislocation density (δ) and micro strain (ε)of the samples were determined from the (002) peak by using the (4.1), (4.2) and (4.3) equations [92,93].

$$L = \frac{0.94\lambda}{\beta\cos\theta} \quad \text{.....} \quad (4.1)$$

$$\delta = 1/L^2 \quad \text{.....} \quad (4.2)$$

$$\varepsilon = \frac{\beta}{4\tan\theta} \quad \text{----------} \quad (4.3)$$

Eqn. (4.1) represents Scherrer formula, where λ = wavelength of the x-ray, θ=angle of diffraction and β= full width at half-maximum of the diffraction peak.

Table. 4.1 and Fig. 4.8 shows different parameters based on structure of MoS_2 NF and MoS_2/MnO_2 nanocomposites and effect of MnO_2 concentration on those parameters, respectively. We determined the full width at half maxima (β) at (002) diffraction peak and found that it increases with the increased concentration of MnO_2 [94-96]. Also observed that crystallite size of the NF decreases from 7.51nm to 5.59nm when the concentration of MnO_2 increases from 2wt% to 6wt%

because the presence of MnO_2 nanorods help to grow cross-linked MoS_2 nanosheets [97,98]. Micro strain and dislocation density are increasing with the concentration of MnO_2.Increased Micro strain has broadened the diffraction line and generated defects, like dislocation generation, imperfect crystal structure and vacancies [99]. From Fig. 4.8 increased dislocation density confirms distortion of lattice and distance between interlayer increases which helps fast ion transportation on the electrode surface [100]. Using following equations

$$\frac{1}{d^2} = \frac{4}{3}\frac{h^2 + hk + k^2}{a^2} + \frac{l^2}{c^2}$$

$$d = \frac{\lambda}{2sin\theta}$$

The value of lattice constants was calculated. Where a, b, c denotes lattice constants, d=atomic plane spacing, λ= wavelength (1.5406 Å), (h, k, l) denotes miller indices, θ=incident angle. The calculated values (in Table 4.1) of lattice constants are less than standard values which represents less volume of lattice cell [101]. Increased dislocation density, smaller crystallite size, difference in d spacing create lattice distortion as a result defect in lattice occurs which gives profound active sites with improved surface area and at the time of charging/discharging charge transfer rate increases between active materials and solution [102-106].

Table 4.1

Diffraction parameters of pristine MoS_2 NF and MoS_2/MnO_2 nanocomposites obtained from XRD analysis.

Samples	B (radian)	L (nm)	d(Å) (002)	d(Å) (100)	a = b (Å)	c (Å)	Micro Strain ε $\times 10^{-3}$	Dislocation Density δ × 10^{-3} (nm^{-2})
MoS_2	1.12	7.51	6.30	2.672	3.08	12.60	39.41	17.71
MoS_2/MnO_2(2wt%)	1.30	6.40	6.35	2.675	3.09	12.70	46.65	20.07
MoS_2/MnO_2(4wt%)	1.34	6.23	6.34	2.671	3.08	12.68	47.85	20.61
MoS_2/MnO_2(6wt%)	1.49	5.59	6.37	2.674	3.09	12.75	53.58	23.01

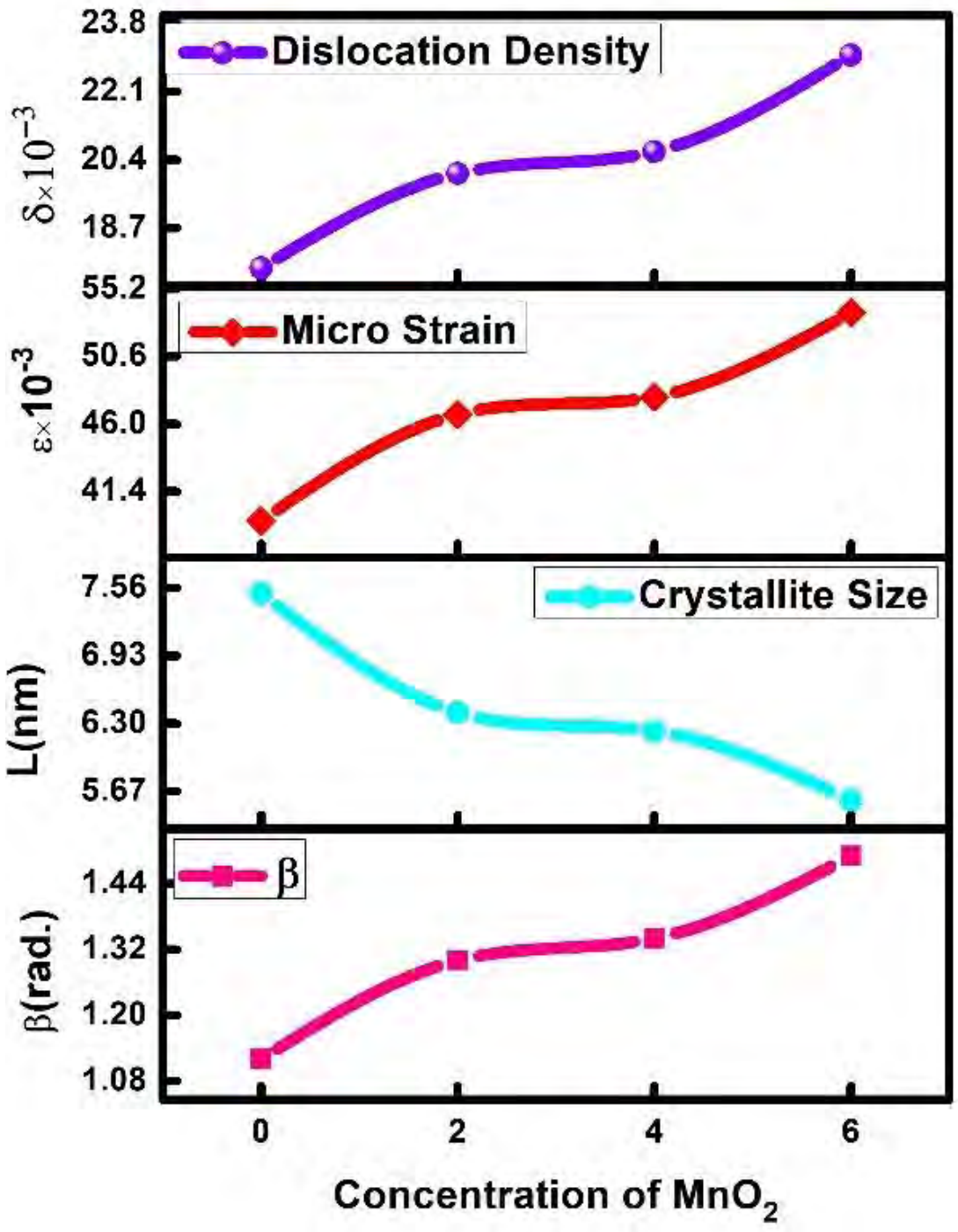

Fig. 4.8 Different XRD parameters variation as a function of MnO_2 Concentration**.**

4.4 Electrochemical performance analysis

4.4.1 Cyclic voltammetry (CV):

CV is an active materials capacitive analysis technique. Ideal capacitive behavior stands for voltammogram's rectangular shape and symmetric current response. MoS_2 nanoflower & MoS_2/MnO_2 nanocomposites were analyzed with the applied potential in the range of -0.3 to 0.2 V at the scan rates of 5, 10, 20, 30,40,50 and 70 mVs^{-1}. Fig. 4.9(a-d) shows CV plots for MoS_2, MoS_2/MnO_2(2wt%), MoS_2/MnO_2(4wt%) & MoS_2/MnO_2(6wt%). The CV curve of the MoS_2 nanoflower & MoS_2/MnO_2 nanocomposite is rectangular-type profile denotes the contribution of electrical double layer capacitance and nonfaradaic charging [107,108]. Due to continuous redox reaction no redox peak in CV curves [109].

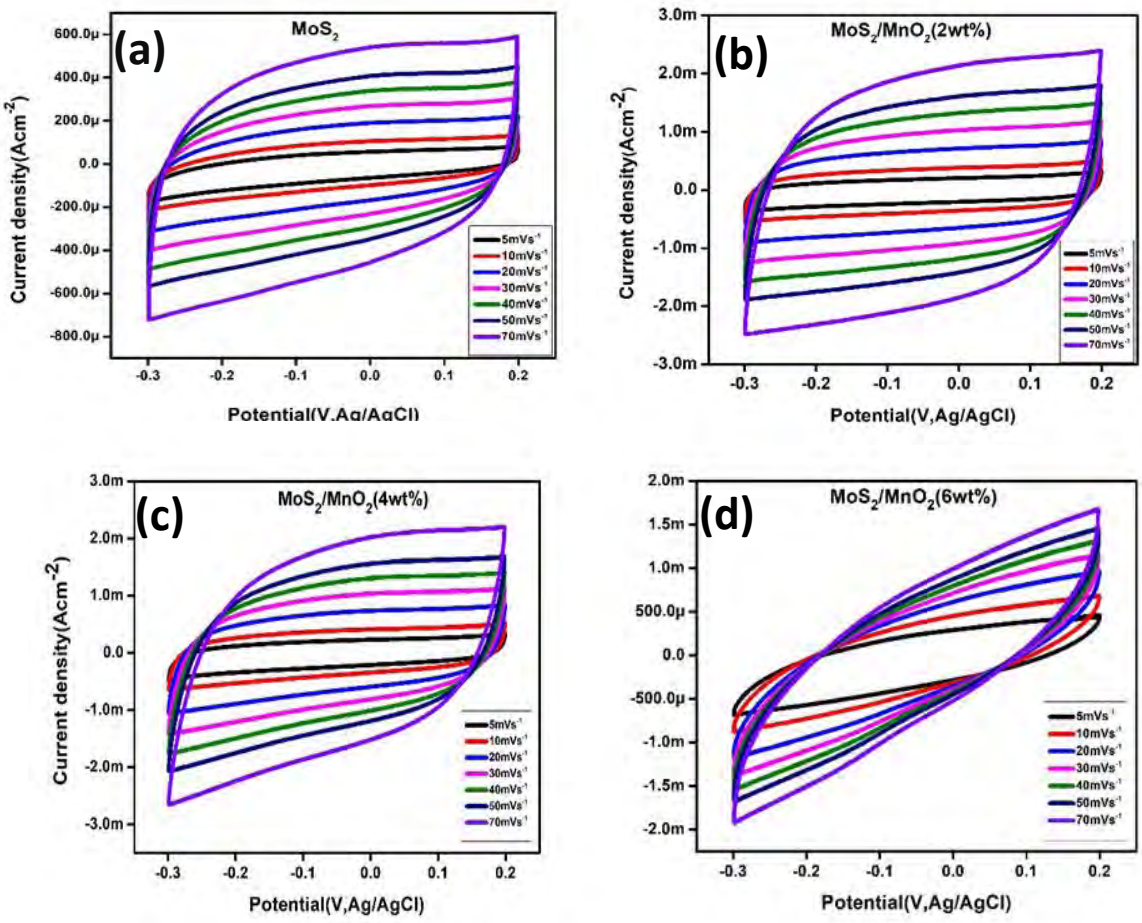

Fig. 4.9 Cyclic voltammetry curves of (a) MoS_2 nanoflower, (b) MoS_2/MnO_2 (2wt%), (c) MoS_2/MnO_2 (4wt%), and (d)MoS_2/MnO_2 (6wt%) nanocomposites at different scan rates.

MoS_2/MnO_2 nanocomposite had larger areas and more symmetrical shape CV plots than pure MoS_2 nanoflower which indicate higher capacitance of the nanocomposites and valuable electrochemical reversibility. At -0.3V voltage CV plots for the nanocomposite has a sharp rise of current that drops sharply at 0.2V which indicates better electrochemical stability of the electrode active material [109-111]. Diffusion layer size changes above the electrode surface as a result low sweep rates took a longer time to record a voltammogram as compared to fast scan rate [107]. Slower sweep rates allow ions to diffuse into interlayers and relatively slow ion adsorption is able to dominate the capacitance [108,112]. The CV area increases with increasing the sweep rate, indicating good rate ability and good capacitance retention at high scan rates [113]. The current densities of CV curves enhance with the increased sweep rates, suggesting the effective utilization of active electrode material by electrolyte ions in the process of electrochemical reaction [114]. When sweep rate increased , specific capacitance decreased because of i)supply ions transportation limitation ,ii) inner active sites in the active material that cannot sustain the redox transitions which could be attributed to diffusion of ions within the electrode ,iii)some portion of electrode surface are inaccessible at high charging–discharging rates [110,115]. Na^+ cation has a great impact on the charge–discharge electrochemistry of MoS_2NF and MoS_2/MnO_2 nanocomposite. A mechanism could be suggested as follows:

$$MoS_2 + Na^+ + e^- \leftrightarrows (MoS_2)^- Na^+_{(surface)} \quad (4.4)$$

$$(MoS_2/MnO_2)_{surface} + Na^+ + e^- \leftrightarrows ((MoS_2/MnO_2)^- Na^+)_{surface} \quad (4.5)$$

$$MoS2 + Na^+ + e^- \leftrightarrows MoS - SNa \quad (4.6)$$

$$MoS_2/MnO_2 + Na^+ + e^- \leftrightarrows (MoS_2/MnO_2)Na_{(intercalation)} \quad (4.7)$$

where eqn(4.4) and eqn(4.5) represents the surface adsorption of Na^+ on the MoS_2 NF and MoS_2–MnO_2 nanocomposite and eqn(4.6) and eqn(4.7) represents the reversible intercalation/de-intercalation of Na^+ in the MoS_2–MnO_2 nanocomposite [82,110].

In Fig. 4.9(d) deviation from the rectangular shape can be attributed to the presence of pseudocapacitance due to MnO_2 present in the system [111]. All the scan rates CV curves showed leaf like structure without any redox peaks indicating that electrode material possess good electrical double-layer capacitance [116]. The reason can be explained as follows: (1) synergistic effect (2) the aggregation-resistant property of such 3D structure allows them to retain a high

accessible surface area with lots of active reaction sites and offer a short path for ion diffusion [113].

Fig. 4.11(a) shows the CV measurements for MoS_2 NF and MoS_2/MnO_2 nanocomposites at a scan rate of 5 mVs^{-1}. Notably, the quasi rectangular area of CV curves of MoS_2/MnO_2 was larger than that of pure MoS_2 NF, indicating the better capacitive performance of MoS_2/MnO_2 nanocomposites. Furthermore, the area of the CV curves decreases with the amount of MnO_2 nanorod in the composite which implied that MnO_2 played key roles in resisting up carriers' transportation in the nanocomposite [111].

4.4.2 Galvanostatic charging-discharging(GCD)

Galvanostatic charge discharge (GCD) measurements were performed between -0.30 V to 0.20 V at various current densities to verify the super capacitive performance of MoS_2 NF and MoS_2/MnO_2 nanocomposite materials (Fig.4.10(a-d)). From the GCD curves it can be seen that all the curves slightly deviate from the symmetric and triangular shape with insignificant iR drop which indicates high reversibility of the materials and those results confirm the pseudocapacitive nature of all the samples. The specific capacitances(Cs) were also determined by GCD plots according to following relation [29],

$$Cs = \frac{i\Delta t}{m\Delta V} \quad \text{----------} \quad (4.8)$$

where i= discharge current, Δt = discharge time, m = mass of the active material and ΔV = potential window width. The specific capacitance of the samples, calculated from the GCD curves using Eq. (4.8), as a function of discharge current densities are shown in Fig. 4.12. It was observed that the discharging time of the nanocomposite increases with the concentration of MnO_2 nanorods, suggesting improvement of the capacitive behavior of MoS_2NF. It can be seen that, as the current density increases, the charging and discharging times decrease, because surface adsorption and diffusion of electrolyte ions become slower into the electrode active material, which results to a decrease in the specific capacitances of the electrodes [29,117,118].

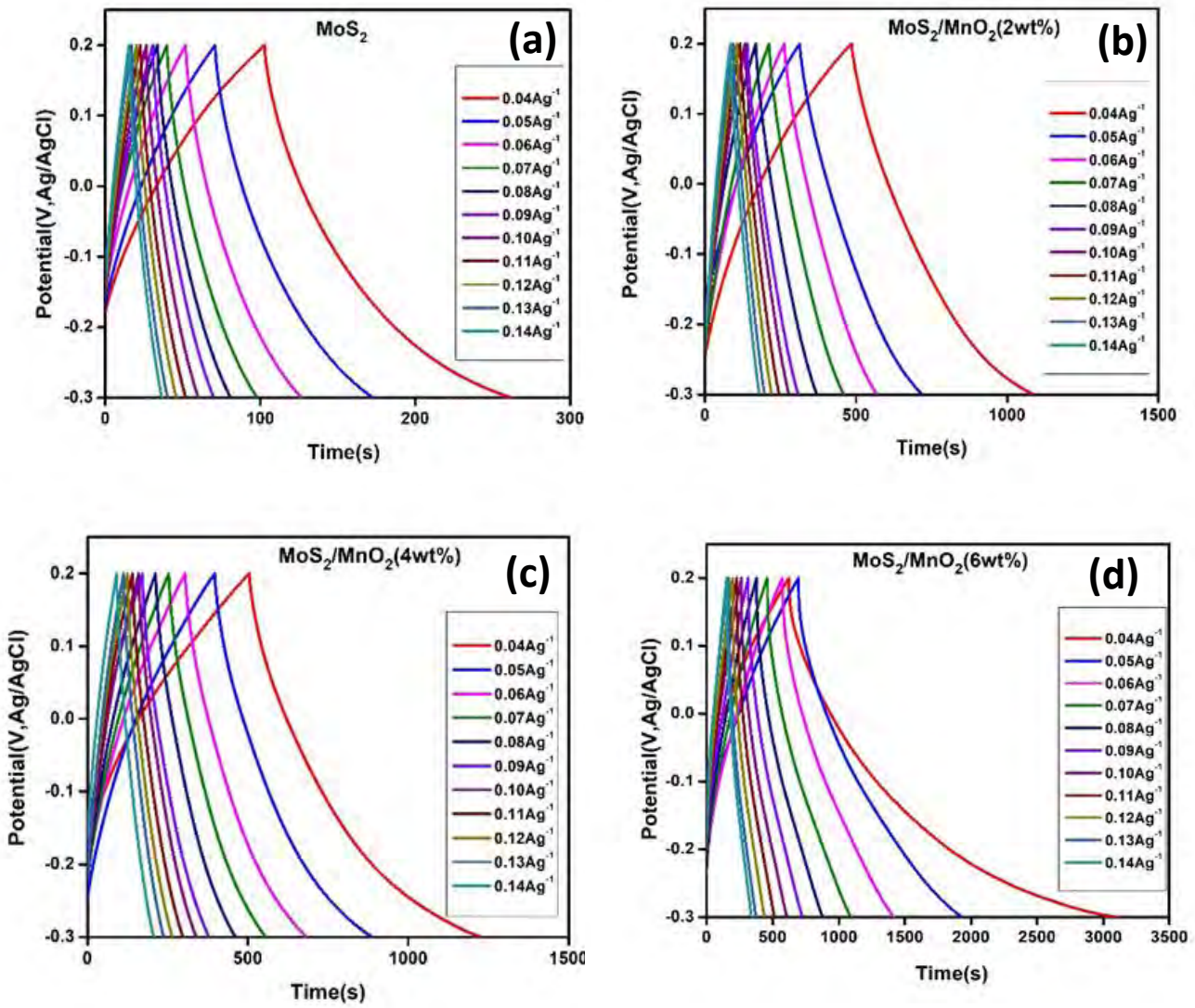

Fig. 4.10 Galvanostatic charging- discharging curves of (a) MoS_2 nanoflower, (b) MoS_2/MnO_2 (2wt%), (c) MoS_2/MnO_2 (4wt%), and (d)MoS_2/MnO_2 (6wt%) nanocomposites at different current densities.

Here outer active surface is responsible for charge storage. At low current density, current accumulating becomes slower, as a result access of active sites on the electrode increases where electrolyte ions can easily diffuse and give complete insertion/extraction reaction and we get better specific capacity [117-119]. Fig. 4.11(b)shows GCD curves of all samples at 0.05 Ag^{-1} current density to compare their electrochemical performances. We observe that MoS_2/MnO_2(6wt%) nanocomposite has much higher discharging time than others and shows highest specific capacitance among all the samples. The specific capacitance (Fig. 4.14) obtained from the GCD curves was 199.12 Fg^{-1} for MoS_2/MnO_2 (6wt%), 57.74 Fg^{-1} for MoS_2/MnO_2 (4wt%),48.11 Fg^{-1} for MoS_2/MnO_2 (2wt%) at the 0.04Ag^{-1} current density , while the specific capacitance of the MoS_2 NF was only 12.73 Fg^{-1}. The incorporation of MnO_2 nanorods in MoS_2 NF gives a surface area

which is electrochemically active for charge transfer and decreased the ion diffusion length during the charge/discharge process, while, MoS_2 NF paves the way for electrolyte ions to enter the active material by minimizing the inactive volume [120]. In the GCD curve iR drop during discharging gives an idea about the internal resistance characteristics of electrode [121]. At a high discharge current density of $0.14Ag^{-1}$, for MoS_2, MoS_2/MnO_2 (2wt%), MoS_2/MnO_2 (4wt%) and MoS_2/MnO_2 (6wt%) short discharge occur between 0.2V to 0.1V ,0.2V to 0.15V,0.2V to 0.15 and 0.2V to 0.175, respectively, because of electrical double-layer capacitance. Faradaic capacitance and electric double layer capacitance is responsible for longer discharge occur between 0.1V to -0.2V,0.15V to -0.2V, 0.15V to -0.2V, 0.175V to -0.2V, respectively [121]. MoS_2/MnO_2 (6wt%) nanocomposite has the lowest iR drop among the nanocomposites suggesting very less internal resistance of the active materials. At a high discharge current density of $0.14Ag^{-1}$ there is no significant iR drop caused by equivalent series resistance, confirms a better capacitive performance [122]. In time of charging-discharging energy dissipation got eliminated for lower internal resistance material, as a result energy storage performance improves. So, to fabricate power-saving supercapacitors, MoS_2/MnO_2 (6wt%) nanocomposite is more preferable [121].

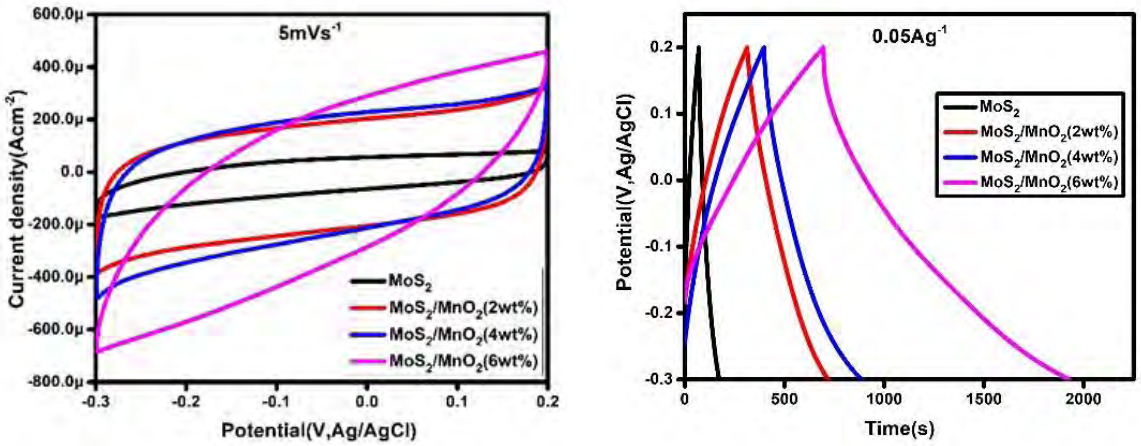

Fig. 4.11 MoS_2 NF and MoS_2/MnO_2 nanocomposites (a)Cyclic voltammetry measurements at 5mV/s (b) Constant-current charge-discharge voltage profiles at 0.05 Ag^{-1}.

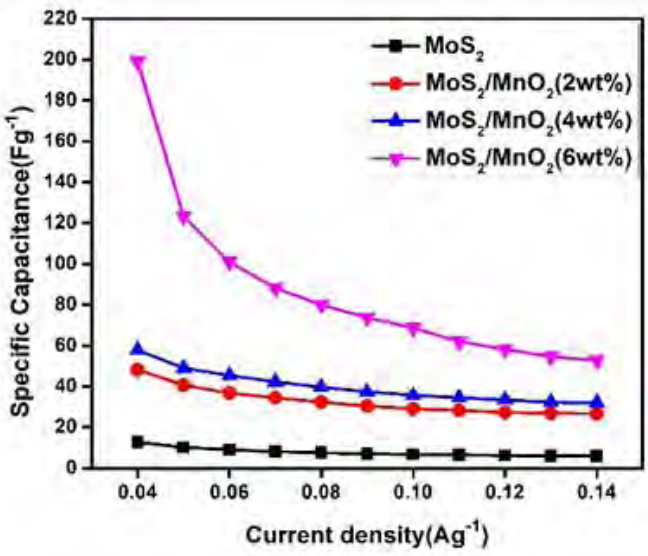

Fig. 4.12 Specific capacitance of MoS_2 NF and MoS_2/MnO_2 nanocomposites at different current density.

Power density and Energy density has an important effect in practical device of energy storage. Power density (Wkg^{-1}) and energy density ($Whkg^{-1}$) were calculated from GCD curves of the synthesized samples by using Eq. (4.9) and Eq. (4.10) [123],

$$E = \frac{1}{2\times3.6} Cs\Delta V^2 \ldots\ldots\ldots\ldots\ldots\ldots\ldots(4.9)$$

$$P = \frac{E}{\Delta t} \times 3600 \ldots\ldots\ldots\ldots\ldots\ldots\ldots\ldots\ldots\ldots(4.10)$$

where Cs=Specific capacitance, ΔV= potential window width and Δt= discharge time

Fig. 4.13 shows Ragone plot (power density vs energy density) for MoS_2/MnO_2 nanocomposite samples. The values are in the supercapacitor region [124]. We observed that for MoS_2/MnO_2(6wt%) nanocomposite highest energy density is 6.91 $Whkg^{-1}$ at power density of 10 WKg^{-1} which is 245.5%,313.77% and 1470.45% higher than MoS_2/MnO_2(4wt%), MoS_2/MnO_2(2wt%) and MoS_2, respectively.

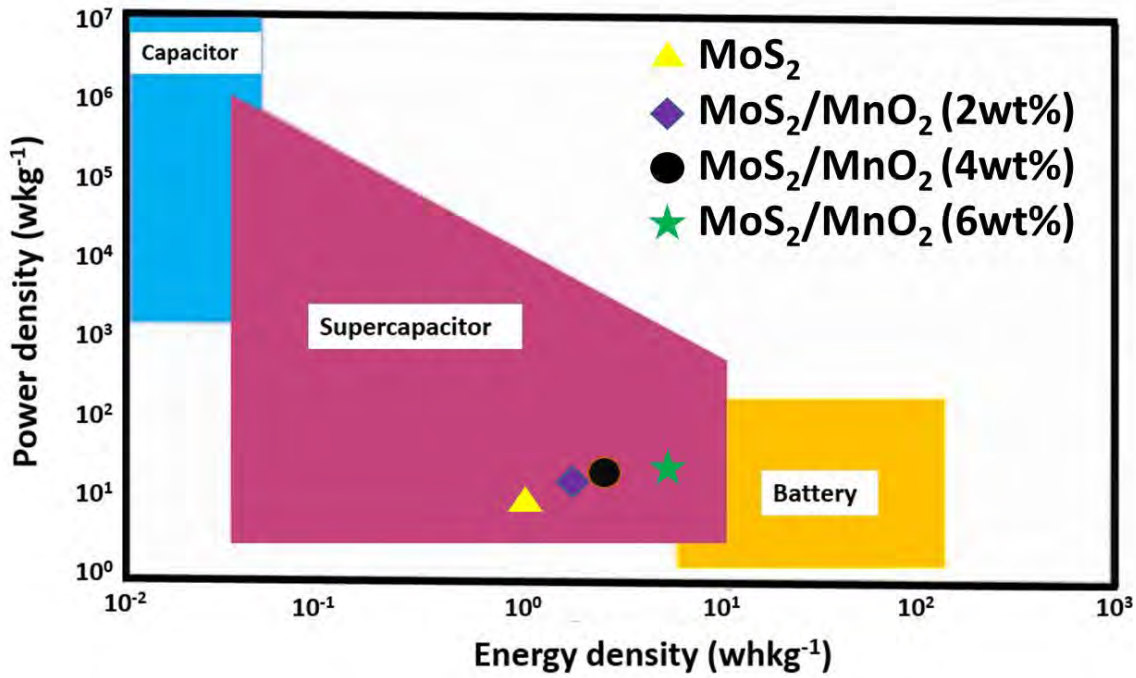

Fig. 4.13 Ragone plot (power density vs energy density) for MoS_2/MnO_2 nanocomposite samples.

4.4.3. Electrochemical impedance spectroscopy(EIS)

Electrochemical impedance spectroscopy (EIS) was performed to investigate the capacitive and resistive properties of the MoS_2 NF and MoS_2/MnO_2 (2wt%,4wt%,6wt%) nanocomposite electrodes in 0.1 Hz–100 kHz frequency range. Fig. 4.14(a) and Fig. 4.14(b) shows the Nyquist plots of all the prepared samples and magnified plot of high frequency zone, respectively. In Nyquist plot, for supercapacitor, semicircular portion at high frequency denotes an intrinsic resistance of electrodes, in the middle frequency (Warburg region) it represents interaction between material porosity and electrolyte ions and at low frequency sudden increment in the values of impedance imaginary part represents its capacitive property, it also can be denoted double-layer capacitive region [125]. The interception point at real impedance axis in the high frequency area determines effective series resistance value, can be represented as solution resistance (Rs) which represents the combination of electrolyte ionic resistance, the substrate intrinsic resistance and contact resistance [126]. It can be seen from EIS curves that MoS_2 NF and MoS_2/MnO_2 (2wt%) nanocomposite has an interception point at real impedance axis in the high frequency zone, respectively ,but MoS_2/MnO_2 (4wt%) and MoS_2/MnO_2 (6wt%) nanocomposite has no interception

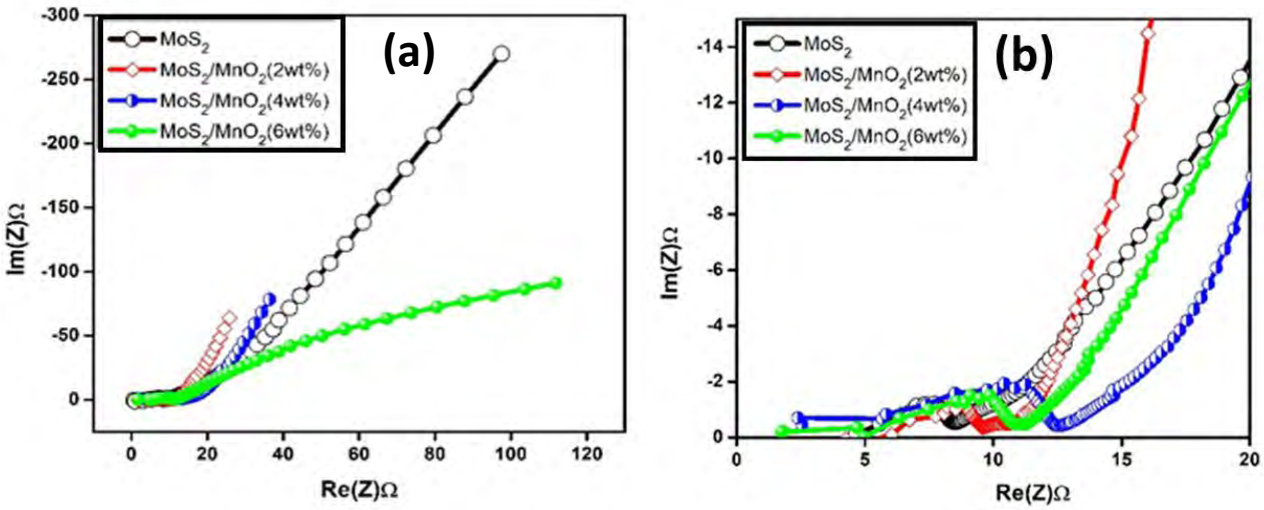

Fig. 4.14 (a)Nyquist plots of MoS_2 NF and as prepared MoS_2/MnO_2 nanocomposites

(b) Nyquist plots of MoS_2 NF and as prepared MoS_2/MnO_2 nanocomposites at high frequency region

point. This suggest that MoS_2 NF and MoS_2/MnO_2 (2wt%) nanocomposite has more solution resistance than MoS_2/MnO_2 (4wt%) and MoS_2/MnO_2 (6wt%) nanocomposite [29]. The result also indicates that increased concentration of MnO_2 has given better charge collection ability and faster ion transportation between electrode active materials and electrolyte [107]. In Fig. 4.15 an equivalent circuit is shown and after fitting the impedance spectra, shown in Fig. 4.16, equivalent circuit parameters were determined, listed in Table. 4.2. Here, Rs = solution resistance, *R*ct = charge transfer resistance, and *W*=Warburg impedance. CPE =Constant phase element, is used in this model in place of a capacitor to compensate for non-homogeneity in the system and also represents the nonideal capacitive property ,as, in the microscopic level electrode surface is porous and rough [127]. In fact, this rough and porous surface can cause a double-layer capacitance to appear as a constant phase element with a CPE-P value between 0.9 and 1 and from Table. 4.2 it can be seen that the CPE-P value of our nanocomposite samples satisfy the range. Quasi-semicircles and low charge transfer resistance (Rct) for all synthesized samples, is the result of faradaic redox reactions and double-layer capacitance on the surface of the electrode [126].

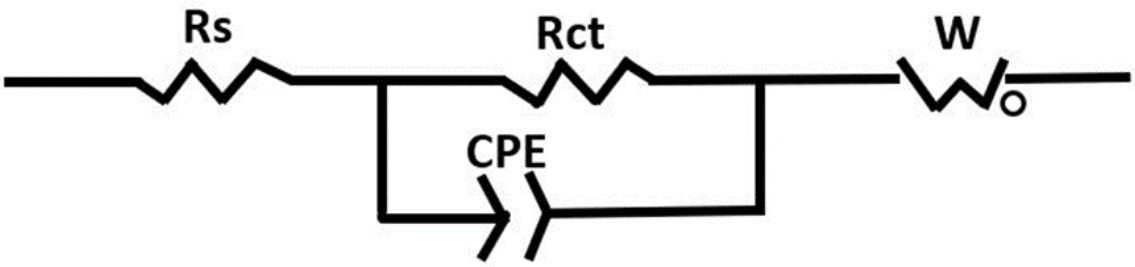

Fig. 4.15 Equivalent circuit diagram of Randle's model.

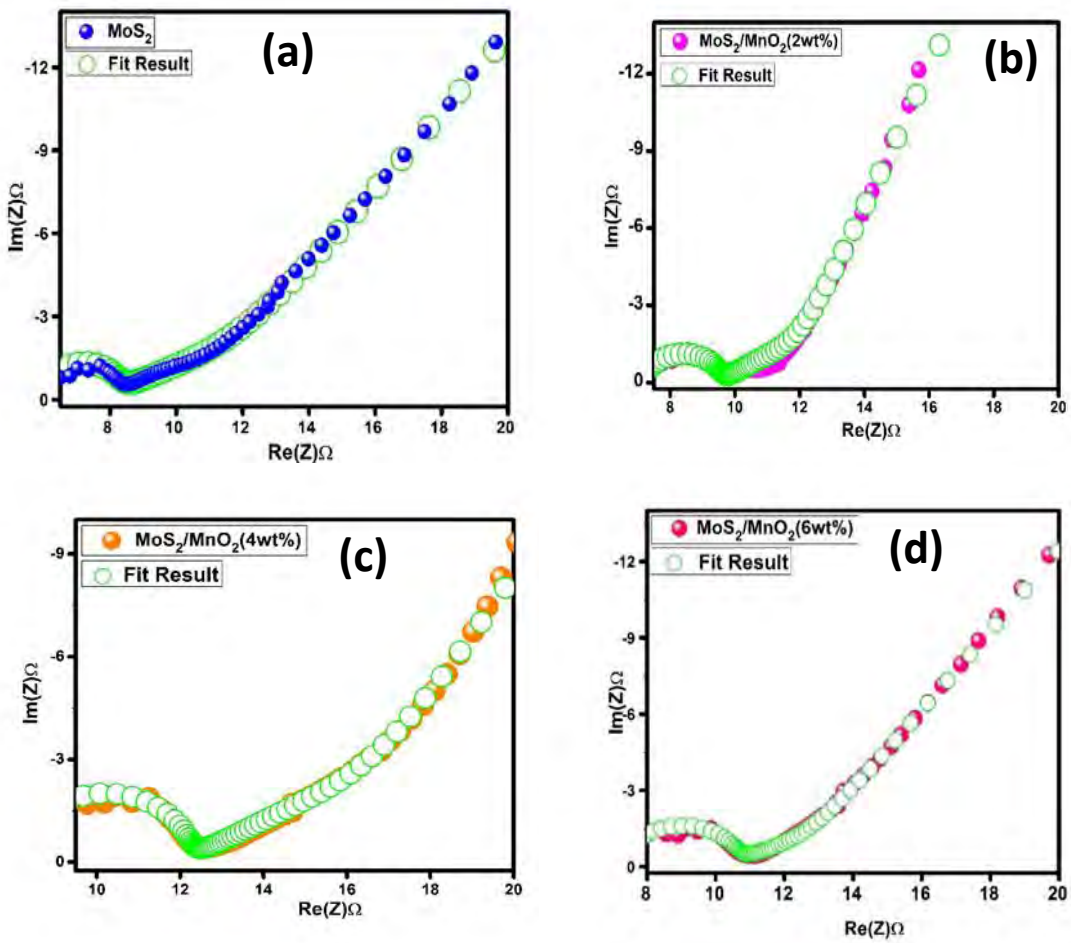

Fig 4.16 Simulated and experimental Nyquist plots of MoS_2 NF and as prepared MoS_2/MnO_2 nanocomposites

From Table. 4.3 it can be observed that Rct(Ω)value of MoS_2/MnO_2 (6wt%) has reduced and CPE-T(μF) value has increased than MoS_2 NF and MoS_2/MnO_2 (2wt%), MoS_2/MnO_2 (4wt%)

nanocomposite, that indicates good electrical conductivity, high wettability, higher rate capability , increased reaction rates of electrode and better efficiency [128,129]. Due to enlarge interlayer distance of MoS_2/MnO_2 (6wt%) nanocomposite, electrolyte gets easy access as a result charge transfer resistance decreases [130]. The value of W_o-R(Ω) for MoS_2/MnO_2 (6wt%) is relatively much smaller. Reduced diffusive resistance gives better cycling performance of the MoS_2/MnO_2 (6wt%) nanocomposite at the time of electrochemical stability test [131]. From XRD data (Table.4.1) MoS_2/MnO_2 (6wt%) nanocomposite has highest amount of dislocation density. Improvement in double layer capacitive property occurs due to higher dislocation density. Increased dislocation density reduces charge transfer resistance because of smaller phase angle, so faster electron movement occurs between active material and electrolyte [127,130].

So, from the EIS data we get that MoS_2/MnO_2 (6wt%) nanocomposite electrode gives superior supercapacitor property than those of the other electrodes and this result is consistent with the results obtained from CV and GCD.

Table. 4.2 EIS fitting parameters of pristine MoS_2 and MoS_2/MnO_2 nanocomposites.

Sample	Rct(Ω)	CPE-T(μF)	CPE-P	W_o-R(Ω)
MoS_2	2.6	0.0835	0.99	10.16
MoS_2/MnO_2(2wt%)	2.55	0.252	0.95	6.55
MoS_2/MnO_2(4wt%)	3.1	0.260	0.98	11
MoS_2/MnO_2(6wt%)	2.5	0.3309	1	5.93

4.4.4 Electrode stability analysis

As MoS_2/MnO_2(6wt%) nanocomposite shows better capacitive performance that's why to check it's cyclic stability 10,000 cycles of charging-discharging operation was done at a current density of $0.17Ag^{-1}$. From Fig. 4.17(a) we observed that just after 3000 cycles retention was reduced to around 82% and then it reached to 100% at around 7000 cycles and again started to decrease after 8000 cycles and finally it was 90% after 10,000 cycles. The coulombic efficiency was 106% at 1st cycle and after 10,000 cycle it was 105% which proves excellent stability of MoS_2/MnO_2(6wt%) nanocomposite electrode. Increased wettability, stability in structure and faster ion diffusion may

give superior cycling stability and coulombic efficiency property to the MoS_2/MnO_2(6wt%) nanocomposite [132]. Also the Nyquist plots after 1st cycle and 10000 cycles are shown in Fig. 4.17(b) which demonstrates that semi-circular portion of the impedance spectrum has lower radius after 10,000 cycles. The insets in Fig. 4.17(b) shows the fitted result and the value of equivalent circuit components Rct, CPE-T, CPE-P, W_o-R are shown in Table. 4.3 Rct and W_o-R values are greater for 1st cycle than after 10,000 cycles which indicates creation of more active sites, decrease in resistivity and faster electron conductivity between electrode and solution [84,132,133].

Table. 4.3 EIS fitting parameters of MoS_2/MnO_2 (6wt%) nanocomposite obtained from the 1st and 10,000th cycle.

Cycle	Rct(Ω)	CPE-T(μF)	CPE-P	W_o-R(Ω)
1	3	0.30	1	6.6
10000	1.9	0.33	0.98	6

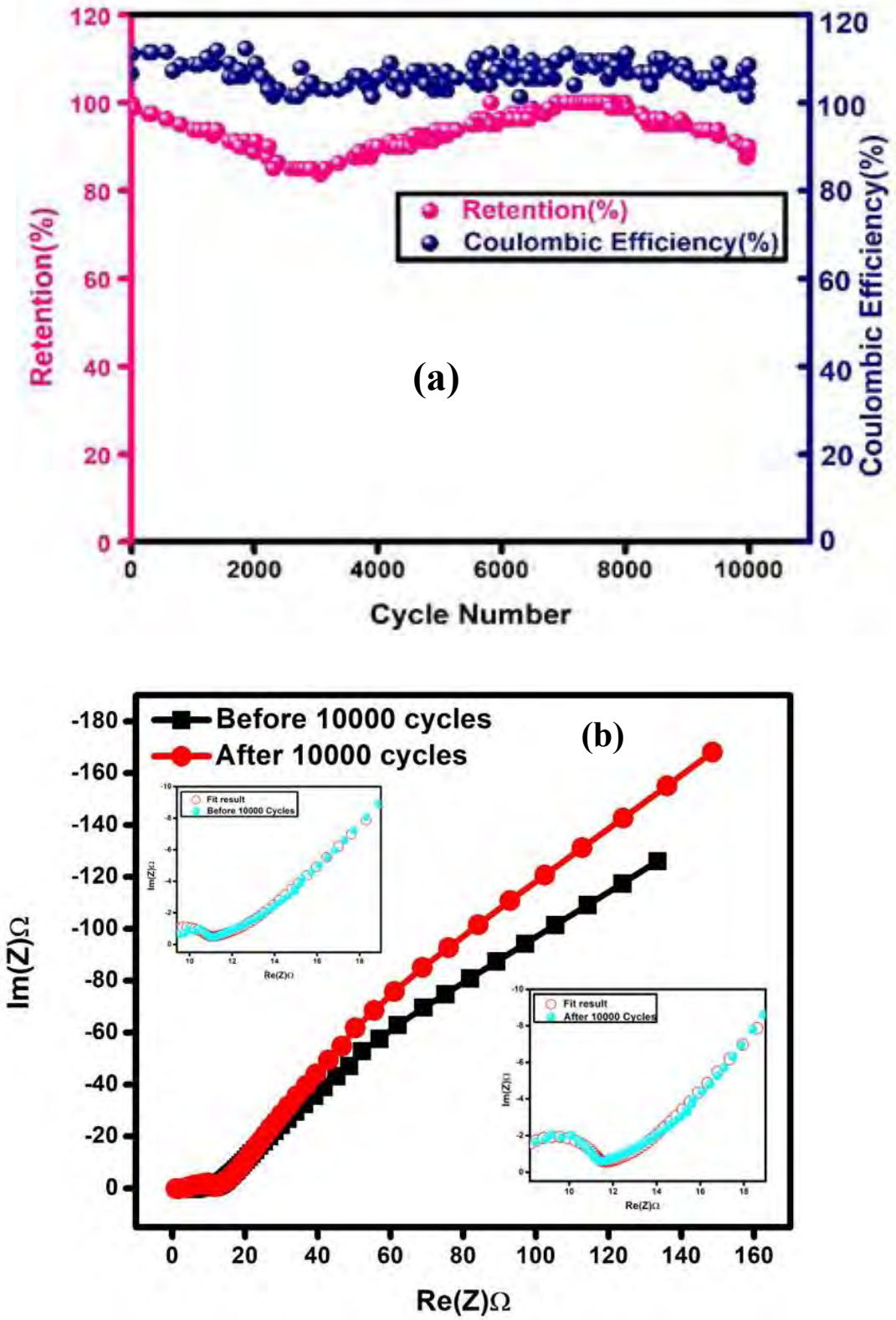

Fig. 4.17. (a) Capacitive retention and Columbic efficiency of the MoS_2/MnO_2 (6wt%) nanocomposite over 10,000cycle of charging-discharging, (b)Nyquist plots of MoS_2/MnO_2 (6wt%) nanocomposite before and after 10,000 cycles of charging-discharging. Inset images show simulated and experimental Nyquist plot.

4.4.5 Electrochemical behavior of MoS_2/MnO_2 (6wt%) as electrode

The CV curve shows that the capacitance value rises as the MnO_2 wt% increases. The GCD curve displays a performance pattern that is similar to that. This implies that the MnO_2 content affects electrochemical performance significantly. The enhanced surface area, larger interplanar spacing, dislocation density, and defect-rich structure of the composite structure may also contribute to this better outcome from the MoS_2/MnO_2 (6%) nanocomposite. The interplanar spacing of the MoS_2 nanoflowers is increased by the incorporation of MnO_2 nanoparticles, resulting in the defect-rich structure. This increased interplanar spacing may provide more open channels for the diffusion of ions and electrons to the electrode interface while also improving the electrical conductivity of the MoS_2 lattice. The transport of electrons and ions from the electrolyte to the electrode surface is restricted by the lower concentration of MnO_2 (2%, 4%). The changes in crystallite size are what cause the capacitance value to rise with MnO_2 concentration. The MoS_2/MnO_2 (6%) nanocomposites have the largest surface area and the smallest crystallite size, which provides more active surface sites for electrochemical reactions. However, as MnO_2 amount is increased, the crystallite size decreases and the surface area of the reaction sites increases. However, when the amount of MnO_2 increases, the size of the crystallite decreases, limiting the number of reaction sites. Additionally, the concentration of MnO_2 (6%) in MoS_2 has improved the dislocation density of the produced samples. The largest dislocation density is found in nanocomposite, which also results in an increase in capacitance value. The results and explanation above make it abundantly evident that the MoS_2/MnO_2 (6%) supercapacitor electrode performed optimally in terms of both capacitance and stability.

To compare the results with the literature, Table 4.4 presents the statistics of a MoS_2 based electrode [24,34,35,134-136]. Among all the reported statistics, the MoS_2/MnO_2 (6%) electrode's specific capacitance has the highest value. This work yields better specific capacitance with superior stability than any other mentioned documented data while using nanosheet or nanoparticle-based electrodes, as opposed to prior reported work. We think that the synergistic effect of MoS_2 and MnO_2 nanoparticles, defect-rich structure, improved electrical conductivity, and small crystallite size are responsible for this amazing outcome. More so than nanosheets or flakes, nanoflower offers a larger surface area. We think that this composite has a great deal to offer as a contender for an electrode material.

Table 4.4 Comparison of capacitance of reported MoS_2 based supercapacitors in the literatures.

Electrode material	Electrolyte/ Electrode Composition (mass ratio)	Current Density (A/g)	Specific Capacitance (F/g)	Number of Cycles	Specific Capacitance Retained %	Ref.
MoS_2/ Mn_3O_4	80 : 15: 5	1	172	2000	69.3	[35]
MoS_2 nanospheres//AC		1	65.33			[134]
MoS_2 nanosheet arrays@Ti Plate	1M KCl	.5	153.5			[135]
MoS_2-G	1 M Na_2SO_4	5	130	1000	92.3	[136]
MoS_2 nanowires/ $NiCo_2O_4$//Active Carbon (AC)		6	21	8000	98.2	[34]
MoS_2-CNT	1M Na_2SO_4	2	74			[24]
MoS_2-MnO_2(6wt%)	0.5Na_2SO_4	.04	199.12	10000	90	This work

CHAPTER 5

CONCLUSIONS

5.1 Conclusions

In conclusion, we have developed a simple hydrothermal process for producing MnO_2 nanoparticles that are integrated into 3D-MoS_2 nanoflower architectures with a range of MnO_2 concentrations (0, 2, 4, and 6 wt%). MoS2 and MoS_2/MnO_2 were evaluated in terms of their surface morphology, structural, optical, and electrochemical characteristics. According to the SEM investigation, the as-prepared MoS_2 and MoS_2/MnO_2 displayed 2H semiconductive phase in the form of nanoflowers. The MoS_2 nanoflower was found to be assembled from a few layer petals by TEM examination. Due to their nanoscale thickness, the petals are discovered to be twisted and overlapping. Using HRTEM examination, the interlayer spacing of the generated samples was determined. MoS_2/MnO_2 (6wt%) exhibits an expanded interlayer lattice spacing of 0.67 nm. The XRD analysis was used to estimate the different structural parameters of the nanoflowers, including crystallite size, lattice strain, micro stain, dislocation density, cell volume, etc. Lattice strain, micro strain, and dislocation density were found to vary with MnO_2 concentration, with MoS_2/MnO_2 (6wt%) achieving the lowest 5.59 nm crystallite size and highest dislocation density. The MoS_2/MnO_2 nanocomposites demonstrate improved capacitance and cycle life than that of MoS_2. It was found that, among all synthesized MoS_2/MnO_2 nanocomposite, for the MoS_2/MnO_2(6wt%) nanocomposite, highest specific capacitance was obtained and value was 199.12Fg^{-1} at a current density of 0.04 Ag^{-1} when energy density was 6.91 $Whkg^{-1}$ at power density of 10 WKg^{-1}. At a current density of 0.17Ag^{-1}, after 10,000 charge/discharge cycles the MoS_2/MnO_2(6wt%) nanocomposite provides 90% capacitance retention which confirms tremendous cycling stability. The higher capacitance of the MoS_2/ MnO_2 electrode than bare MoS_2 electrode denotes larger specific surface area, greater interlayer spacing, higher wettability faster intrinsic electrical conductivity, improved electrolytic cation intercalation at the interface and overall defect-rich structure. So, to prepare high performance stable supercapacitor this experiment can provide significant insights.

5.2 Suggestions for Future Work

To further comprehend the characteristics and potential of MoS_2 and MoS_2/MnO_2 nanocomposite, the following characterization may be carried out:

- The elemental analysis of the as-prepared MoS_2 and MoS_2/MnO_2 nanocomposites will be done using XPS.
- Effect of more weight% of MnO_2 nanorod in MoS_2 NF will be examined.
- Electrochemical performance will be analyzed by two electrode system.
- Charcoal will be used with the nanocomposite to measure the specific capacitance.
- Those prepared nanocomposite will be used in Coin cells.

REFERENCES

[1] Simon, P. and Gogotsi, Y. "Materials for electrochemical capacitors." *Nature materials*, Vol 7(11), pp.845-854, (2008).

[2] Liu, P.Y., Zhao, J.J., Dong, Z.P., Liu, Z.L. and Wang, Y.Q. "Interwoving polyaniline and a metal-organic framework grown in situ for enhanced supercapacitor behavior." *Journal of Alloys and Compounds*, Vol 854, pp.157181, (2021).

[3] Prakash, D. and Manivannan, S. "Unusual battery type pseudocapacitive behaviour of graphene oxynitride electrode: High energy solid-state asymmetric supercapacitor." *Journal of Alloys and Compounds*, Vol 854, pp.156853, (2021).

[4] Zan, G., Wu, T., Chen, H., Dong, F. and Wu, Q. "$BiVO_4$ nanocoral superstructures and their excellent electrical/optical dual-functions." *Journal of Alloys and Compounds*, Vol 852, pp.157035, (2021).

[5] Lu, H. and Zhao, X.S. "Biomass-derived carbon electrode materials for supercapacitors." *Sustainable Energy & Fuels*, Vol 1(6), pp.1265-1281, (2017).

[6] Zhang, J. and Zhao, X.S., "On the configuration of supercapacitors for maximizing electrochemical performance." *ChemSusChem*, Vol 5(5), pp.818-841, (2012).

[7] Gogotsi, Y. and Simon, P. "True performance metrics in electrochemical energy storage." *science*, Vol 334(6058), pp.917-918, (2011).

[8] Xu, C., Xu, B., Gu, Y., Xiong, Z., Sun, J. and Zhao, X.S. "Graphene-based electrodes for electrochemical energy storage." *Energy & Environmental Science*, Vol 6(5), pp.1388-1414, (2013).

[9] Zhong, Y., Xia, X., Shi, F., Zhan, J., Tu, J. and Fan, H.J. "Transition metal carbides and nitrides in energy storage and conversion." *Advanced science*, Vol 3(5), pp.1500286, (2016).

[10] Wang, Y.H., Huang, K.J. and Wu, X. "Recent advances in transition-metal dichalcogenides based electrochemical biosensors: A review." *Biosensors and Bioelectronics*, Vol 97, pp.305-316, (2017).

[11] Chen, Y.X., Huang, K.J. and Niu, K.X. "Recent advances in signal amplification strategy based on oligonucleotide and nanomaterials for microRNA detection-a review." *Biosensors and Bioelectronics*, Vol 99, pp.612-624, (2018).

[12] Miller, J.R. and Simon, P. "Electrochemical capacitors for energy management." *science*, Vol 321(5889), pp.651-652, (2008)

[13] Oswal, M., Paul, J. and Zhao, R. "A comparative study of lithium-ion batteries." *University of southern California*, pp.2419-2430, (2010).

[14] Lan, D., Chen, Y., Chen, P., Chen, X., Wu, X., Pu, X., Zeng, Y. and Zhu, Z. "Mesoporous CoO nanocubes@ continuous 3D porous carbon skeleton of rose-based electrode for high-performance supercapacitor." *ACS applied materials & interfaces*, Vol 6(15), pp.11839-11845, (2014).

[15] Wang, T., Chen, S., Pang, H., Xue, H. and Yu, Y. "MoS_2-based nanocomposites for electrochemical energy storage." *Advanced science*, Vol 4(2), pp.1600289, (2017).

[16] Yu, Z., Tetard, L., Zhai, L. and Thomas, J. "Supercapacitor electrode materials: nanostructures from 0 to 3 dimensions." *Energy & Environmental Science*, Vol 8(3), pp.702-730, (2015).

[17] Zhang, L.L. and Zhao, X.S. "Carbon-based materials as supercapacitor electrodes." *Chemical Society Reviews*, Vol 38(9), pp.2520-2531, (2009).

[18] Chmiola, J., Yushin, G., Gogotsi, Y., Portet, C., Simon, P. and Taberna, P.L. "Anomalous increase in carbon capacitance at pore sizes less than 1 nanometer." *science*, Vol 313(5794), pp.1760-1763, (2006).

[19] Gu, W. and Yushin, G. "Review of nanostructured carbon materials for electrochemical capacitor applications: advantages and limitations of activated carbon, carbide-derived carbon, zeolite-templated carbon, carbon aerogels, carbon nanotubes, onion-like carbon, and graphene." *Wiley Interdisciplinary Reviews: Energy and Environment*, Vol 3(5), pp.424-473, (2014).

[20] Thounthong, P., Chunkag, V., Sethakul, P., Sikkabut, S., Pierfederici, S. and Davat, B. "Energy management of fuel cell/solar cell/supercapacitor hybrid power source." *Journal of power sources*, Vol 196(1), pp.313-324, (2011).

[21] Chia, X., Eng, A.Y.S., Ambrosi, A., Tan, S.M. and Pumera, M. "Electrochemistry of nanostructured layered transition-metal dichalcogenides." *Chemical reviews*, Vol 115(21), pp.11941-11966, (2015).

[22] Bulakhe, R.N. and Shim, J.J. "Layer-structured nanohybrid MoS_2@ rGO on 3D nickel foam for high performance energy storage applications." *New Journal of Chemistry*, Vol 41(4), pp.1473-1482, (2017).

[23] Choudhary, N., Islam, M.R., Kang, N., Tetard, L., Jung, Y. and Khondaker, S.I. "Two-dimensional lateral heterojunction through bandgap engineering of MoS_2 via oxygen plasma." *Journal of Physics: Condensed Matter*, Vol 28(36), pp.364002, (2016).

[24] Chen, M., Dai, Y., Wang, J., Wang, Q., Wang, Y., Cheng, X. and Yan, X. "Smart combination of three-dimensional-flower-like MoS_2 nanospheres/interconnected carbon nanotubes for application in supercapacitor with enhanced electrochemical performance." *Journal of Alloys and Compounds*, Vol 696, pp.900-906, (2017).

[25] Ghasemi, F., Jalali, M., Abdollahi, A., Mohammadi, S., Sanaee, Z. and Mohajerzadeh, S. "A high performance supercapacitor based on decoration of MoS_2/reduced graphene oxide with NiO nanoparticles." *RSC advances*, Vol 7(83), pp.52772-52781, (2017).

[26] Zhang, Y., He, T., Liu, G., Zu, L. and Yang, J. "One-pot mass preparation of MoS_2/C aerogels for high-performance supercapacitors and lithium-ion batteries." *Nanoscale*, Vol 9(28), pp.10059-10066, (2017).

[27] Zhou, X., Wan, L.J. and Guo, Y.G. "Facile synthesis of MoS_2@ CMK-3 nanocomposite as an improved anode material for lithium-ion batteries." *Nanoscale*, Vol 4(19), pp.5868-5871, (2012).

[28] Cook, J.B., Kim, H.S., Yan, Y., Ko, J.S., Robbennolt, S., Dunn, B. and Tolbert, S.H. "Mesoporous MoS_2 as a transition metal dichalcogenide exhibiting pseudocapacitive Li and Na-ion charge storage." *Advanced Energy Materials*, Vol 6(9), pp.1501937, (2016).

[29] Kanaujiya, N., Kumar, N., Srivastava, A.K., Sharma, Y. and Varma, G.D. "One-step synthesized mesoporous MnO_2@ MoS_2 nanocomposite for high performance energy storage devices." *Journal of Electroanalytical Chemistry*, Vol 824, pp.226-237, (2018).

[30] Shen, Y., Li, Z., Cui, Z., Zhang, K., Zou, R., Yang, F. and Xu, K. "Boosting the interface reaction activity and kinetics of cobalt molybdate by phosphating treatment for aqueous zinc-ion batteries with high energy density and long cycle life." *Journal of Materials Chemistry A*, Vol 8(40), pp.21044-21052, (2020).

[31] Ramesh, S., Karuppasamy, K., Sivasamy, A., Kim, H.S., Yadav, H.M. and Kim, H.S. "Core shell nanostructured of Co_3O_4@ RuO_2 assembled on nitrogen-doped graphene sheets electrode for an efficient supercapacitor application." *Journal of Alloys and Compounds*, Vol 877, pp.160297, (2021).

[32] Liao, X., Zhao, Y., Wang, J., Yang, W., Xu, L., Tian, X., Shuang, Y., Owusu, K.A., Yan, M. and Mai, L. "MoS_2/MnO_2 heterostructured nanodevices for electrochemical energy storage". *Nano Research*, Vol 11, pp.2083-2092, (2018).

[33] Wang, M., Fei, H., Zhang, P. and Yin, L. "Hierarchically layered MoS_2/ Mn_3O_4 hybrid architectures for electrochemical supercapacitors with enhanced performance." *Electrochimica* Acta, Vol 209, pp.389-98, (2016).

[34] Wen, S., Liu, Y., Zhu, F., Shao, R. and Xu, W. "Hierarchical MoS_2 nanowires/$NiCo_2O_4$ nanosheets supported on Ni foam for high-performance asymmetric supercapacitors." *Appl Surface Science*, Vol 428, pp.616-622, (2018).

[35] Zhou, J., Guo, M., Wang, L., Ding, Y., Zhang, Z., Tang, Y., Liu, C. and Luo, S. "1T-MoS_2 nanosheets confined among TiO_2 nanotube arrays for high performance supercapacitor." *Chemical Engineering Journal*, Vol 366, pp.163-171, (2019).

[36] Zhang, Y., He, T., Liu, G., Zu, L. and Yang, J "One-pot mass preparation of MoS_2/C aerogels for high-performance supercapacitors and lithium-ion batteries." *Nanoscale*, Vol 9(28), pp.10059–10066, (2017).

[37] Feng, N., Meng, R., Zu, L., Feng, Y., Peng, C., Huang, J., Liu, G., Chen, B. and Yang, J., "A polymer-direct-intercalation strategy for MoS_2/carbon-derived heteroaerogels with ultrahigh pseudocapacitance." *Nature communications*, Vol 10(1), pp.1372, (2019).

[38] Stephenson, T., Li, Z., Olsen, B. and Mitlin, D. "Lithium ion battery applications of molybdenum disulfide (MoS_2) nanocomposites." *Energy & Environmental Science,* Vol 7(1), pp. 209–231, (2014).

[39] Pomerantseva, E. and Gogotsi, Y. "Two-dimensional heterostructures for energy storage." *Nature Energy*, Vol 2(7), pp.1-6, (2017).

[40] Zhang, X., Lai, Z., Tan, C. and Zhang, H. "Solution-processed two-dimensional MoS_2 nanosheets: preparation, hybridization, and applications." *Angewandte Chemie International Edition,* Vol 55*(*31), pp.8816-8838, (2016).

[41] Wang, X., Ding, J., Yao, S., Wu, X., Feng, Q., Wang, Z. and Geng, B. "High supercapacitor and adsorption behaviors of flower-like MoS_2 nanostructures." *Journal of Materials Chemistry A*, Vol 2(38), pp.15958-15963, (2014).

[42] Wu, Z., Li, B., Xue, Y., Li, J., Zhang, Y. and Gao, F. "Fabrication of defect-rich MoS_2 ultrathin nanosheets for application in lithium-ion batteries and supercapacitors." *Journal of Materials Chemistry A*, Vol 3(38), pp.19445-19454, (2015).

[43] Ahmad, M.H., Alam, R.B., Ul-Hamid, A., Farhad, S.F.U. and Islam, M.R. "Hydrothermal synthesis of Co_3O_4 nanoparticles decorated three dimensional MoS_2 nanoflower for exceptionally stable supercapacitor electrode with improved capacitive performance." *Journal of Energy Storage*, Vol 47, pp.103551, (2022).

[44] He, P., Zhao, X., Zhang, Y., Wu, J., Chen, N., Wei, J. and Xu, T. "Remove elemental mercury from simulated flue gas by flower-like MoS_2 modified with nanoparticles MnO_2." *Chemical Engineering Journal*, Vol 412, pp.128588, (2021).

[45] Sha, R., Gopalakrishnan, A., Sreenivasulu, K.V., Srikanth, V.V. and Badhulika, S. "Template-cum-catalysis free synthesis of α-MnO_2 nanorods-hierarchical MoS_2 microspheres composite for ultra-sensitive and selective determination of nitrite." *Journal of Alloys and Compounds*, Vol 794, pp.26-34, (2019).

[46] Wang, J.G., Kang, F. and Wei, B. "Engineering of MnO_2-based nanocomposites for high-performance supercapacitors." *Progress in Materials Science*, Vol 74, pp.51-124, (2015).

[47] Huang, M., Li, F., Dong, F., Zhang, Y.X. and Zhang, L.L. "MnO_2-based nanostructures for high-performance supercapacitors." *Journal of Materials Chemistry A*, Vol 3(43), pp.21380-21423, (2015).

[48] Duan, X., Yang, J., Gao, H., Ma, J., Jiao, L. and Zheng, W. "Controllable hydrothermal synthesis of manganese dioxide nanostructures: shape evolution, growth mechanism and electrochemical properties." *CrystEngComm*, Vol 14(12), pp.4196-4204, (2012).

[49] Chhowalla, M., Shin, H. S., Eda, G., Li, L. J., Loh, K. P., and Zhang, H. "The chemistry of two-dimensional layered transition metal dichalcogenide nanosheets." *Nat. Chem.,* Vol 5, pp. 263–275, (2013).

[50] Cho, M. H., Ju, J., Kim, S. J., and Jang, H. "Tribological properties of solid lubricants (graphite, Sb_2S_3, MoS_2) for automotive brake friction materials." *Wear*, Vol 260, pp. 855–860, (2006).

[51] Wang, Q. H., Kalantar-Zadeh, K., Kis, A., Coleman, J. N., and Strano, M. S. "Electronics and optoelectronics of two-dimensional transition metal dichalcogenides." *Nature Nanotechnology*., Vol 7, pp. 699–712, (2012).

[52] Benavente, E., Santa Ana, M. A., Mendizábal, F., and González, G. "Intercalation chemistry of molybdenum disulfide." *Coordination chemistry reviews*, Vol 224(1-2), pp. 87–109, (2002).

[53] El-Mahalawy, S. H., and Evans, B. L. "The thermal expansion of 2H-MoS_2, 2H-$MoSe_2$ and 2H-WSe_2 between 20 and 800°C." *Journal of Applied Crystallography*, Vol 9(5), pp. 403–406, (1976).

[54] Eda, G., Fujita, T., Yamaguchi, H., Voiry, D., Chen, M., and Chhowalla, M. "Coherent Atomic and Electronic Heterostructures of Single-Layer MoS_2." *ACS Nano*, Vol 6(8), pp. 7311–7317, (2012).

[55] Wang, X. and Li, Y. "Rational synthesis of α-MnO_2 single-crystal nanorods." *Chemical Communications*, Vol 7, pp.764-765, (2002).

[56] Xiao, W., Wang, D. and Lou, X.W. "Shape-controlled synthesis of MnO_2 nanostructures with enhanced electrocatalytic activity for oxygen reduction." *The Journal of Physical Chemistry C*, Vol 114(3), pp.1694-1700, (2010).

[57] Devaraj, S. and Munichandraiah, N. "Effect of crystallographic structure of MnO_2 on its electrochemical capacitance properties." *The Journal of Physical Chemistry C*, Vol 112(11), pp.4406-4417, (2008).

[58] Frackowiak, E. "Carbon materials for supercapacitor application." *Physical chemistry chemical physics*, Vol 9(15), pp.1774-1785, (2007).

[59] Inagaki, M., Konno, H., and Tanaike, O. "Carbon materials for electrochemical capacitors." *Journal of Power Sources*, Vol 195(24), pp.7880–7903, (2010).

[60] Burke, A. "Ultracapacitors: why, how, and where is the technology." *Journal of Power Sources*, Vol 91, pp. 37–50, (2000).

[61] Ryu, K. S., Kim, K. M., Park, Y. J., Park, N. G., Kang, M. G., and Chang, S. H. "Redox supercapacitor using polyaniline doped with Li salt as electrode." *Solid State Ion*ics, Vol 152–153, pp. 861–866, (2002).

[62] Chuang, C. M., Huang, C. W., Teng, H., and Ting, J. M. "Effects of Carbon Nanotube Grafting on the Performance of Electric Double Layer Capacitors." *Energy & Fuels*, Vol 24, pp. 6476–6482, (2010).

[63] Wang, G., Zhang, L., and Zhang, J. "A review of electrode materials for electrochemical supercapacitors." *Chemical Society Reviews*, Vol 41(2), pp.797–828, (2012).

[64] Simon, P., and Gogotsi, Y. "Materials for electrochemical capacitors." *Nature Materials*., Vol 7(11), pp. 845–854, (2008).

[65] Wang, Y. G., and Zhang, X. G. "All solid-state supercapacitor with phosphotungstic acid as the proton-conducting electrolyte." *Solid State Ionics*, Vol 166(1-2), pp.61–67, (2004).

[66] Majumdar, D. "Recent progress in copper sulfide based nanomaterials for high energy supercapacitor applications." *Journal of Electroanalytical Chemistry*, Vol 880, pp.114825, (2021).

[67] Sharma, P., and Bhatti, T. S. "A review on electrochemical double-layer capacitors." *Energy conversion and management*, Vol 51(12), pp. 2901–2912, (2010).

[68] Belhachemi, F., Rael, S., and Davat, B. "A physical based model of power electric double-layer supercapacitors." in 2000 IEEE Industry Applications Conference. *Thirty-Fifth IAS Annual Meeting and World Conference on Industrial Applications of Electrical Energy*, Vol 5, pp. 3069–3076, (2000).

[69] Ryu, K. S., Kim, K. M., Park, N. G., Park, Y. J., and Chang, S. H. "Symmetric redox supercapacitor with conducting polyaniline electrodes." *Journal of Power Sources*, Vol. 103(2), pp. 305–309, (2002).

[70] Conway, B.E. "Electrochemical supercapacitors: scientific fundamentals and technological applications". *Springer Science & Business Media*, (2013).

[72] Taberna, P.L., Simon, P. and Fauvarque, J.F. "Electrochemical characteristics and impedance spectroscopy studies of carbon-carbon supercapacitors." *Journal of the Electrochemical Society*, Vol 150(3), pp.A292, (2003).

[73] Aguedo, J., Lorencova, L., Barath, M., Farkas, P. and Tkac, J. "Electrochemical impedance spectroscopy on 2D nanomaterial MXene modified interfaces: application as a characterization and transducing tool." *Chemosensors*, Vol 8(4), pp.127, (2020).

[74] Magar, H.S., Hassan, R.Y. and Mulchandani, A. "Electrochemical impedance spectroscopy (EIS): Principles, construction, and biosensing applications." *Sensors*, Vol 21(19), pp.6578, (2021).

[75] Park, B.H. and Choi, J.H. "Improvement in the capacitance of a carbon electrode prepared using water-soluble polymer binder for a capacitive deionization application." *Electrochimica Acta*, *55*(8), pp.2888-2893, (2010).

[76] Park, H.K., Kong, B.S. and Oh, E.S. "Effect of high adhesive polyvinyl alcohol binder on the anodes of lithium ion batteries." *Electrochemistry Communications*, Vol 13(10), pp.1051-1053, (2011).

[77] Wang, X. and Li, Y. "Rational synthesis of α-MnO_2 single-crystal nanorods." *Chemical Communications*, Vol (7), pp.764-765, (2002).

[78] Zhang, X., Huang, X., Xue, M., Ye, X., Lei, W., Tang, H. and Li, C. "Hydrothermal synthesis and characterization of 3D flower-like MoS_2 microspheres." *Materials Letters*, Vol 148, pp.67-70, (2015).

[79] Hu, L., Ren, Y., Yang, H. and Xu, Q. "Fabrication of 3D hierarchical MoS_2/polyaniline and MoS_2/C architectures for lithium-ion battery applications." *ACS applied materials & interfaces*, Vol 6(16), pp.14644-14652, (2014).

[80] Fu, H., Yu, K., Li, H., Li, J., Guo, B., Tan, Y., Song, C. and Zhu, Z. "Enhanced field emission and photocatalytic performance of MoS_2 titania nanoheterojunctions via two synthetic approaches." *Dalton Transactions*, Vol 44(4), pp.1664-1672, (2015).

[81] Bai, X., Tong, X., Gao, Y., Zhu, W., Fu, C., Ma, J., Tan, T., Wang, C., Luo, Y. and Sun, H. "Hierarchical multidimensional MnO_2 via hydrothermal synthesis for high performance supercapacitors." *Electrochimica Acta*, Vol 281, pp.525-533, (2018).

[82] Chai, C., Liu, A., Wang, Y., Lu, Y. and Che, H. "A MoS_2-templated oxidation-etching strategy to synthesize hollow δ-MnO_2 nanospheres as a high-performance electrode for supercapacitor." *Ceramics International*, Vol 44(14), pp.16923-16930, (2018).

[83]. Li, H., Yu, K., Lei, X., Guo, B., Fu, H. and Zhu, Z. "Hydrothermal synthesis of novel MoS_2/$BiVO_4$ hetero-nanoflowers with enhanced photocatalytic activity and a mechanism investigation." *The Journal of Physical Chemistry C*, Vol 119(39), pp.22681-22689, (2015).

[84] Xiong, F., Cai, Z., Qu, L., Zhang, P., Yuan, Z., Asare, O.K., Xu, W., Lin, C. and Mai, L. "Three-dimensional crumpled reduced graphene oxide/MoS_2 nanoflowers: a stable anode for lithium-ion batteries." *ACS applied materials & interfaces*, Vol 7(23), pp.12625-12630, (2015).

[85] Wu, Z., Li, B., Xue, Y., Li, J., Zhang, Y. and Gao, F. "Fabrication of defect-rich MoS_2 ultrathin nanosheets for application in lithium-ion batteries and supercapacitors." *Journal of Materials Chemistry A*, Vol 3(38), pp.19445-19454, (2015).

[86] Wang, J., Zhou, H., Zhu, M., Yuan, A. and Shen, X. "Metal-organic framework-derived Co_3O_4 covered by MoS_2 nanosheets for high-performance lithium-ion batteries." *Journal of Alloys and Compounds*, Vol 744, pp.220-227, (2018).

[87]. Wang, H., Lu, Z., Qian, D., Li, Y. and Zhang, W. "Single-crystal α-MnO_2 nanorods: synthesis and electrochemical properties." *Nanotechnology*, Vol 18(11), pp.115616, (2007).

[88]. Song, H., Tang, A., Xu, G., Liu, L., Pan, Y. and Yin, M. "Hydrothermal synthesis and electrochemical properties of MoS_2/C nanocomposite." *Int J Electrochem Sci*, Vol 13, pp.6708-6716, (2018).

[89]. Fu, H., Yu, K., Li, H., Li, J., Guo, B., Tan, Y., Song, C. and Zhu, Z. "Enhanced field emission and photocatalytic performance of MoS_2 titania nanoheterojunctions via two synthetic approaches." *Dalton Transactions*, Vol 44(4), pp.1664-1672, (2015).

[90]. Lin, X., Wang, X., Zhou, Q., Wen, C., Su, S., Xiang, J., Cheng, P., Hu, X., Li, Y., Wang, X. and Gao, X. "Magnetically recyclable MoS_2/Fe_3O_4 hybrid composite as visible light responsive photocatalyst with enhanced photocatalytic performance." *ACS Sustainable Chemistry & Engineering*, Vol 7(1), pp.1673-1682, (2018).

[91] Du, G., Guo, Z., Wang, S., Zeng, R., Chen, Z. and Liu, H. "Superior stability and high capacity of restacked molybdenum disulfide as anode material for lithium ion batteries." *Chemical communications*, Vol 46(7), pp.1106-1108, (2010).

[92] Radmilovic, V., Gasteiger, H.A. and Ross, P.N. "Structure and chemical composition of a supported Pt-Ru electrocatalyst for methanol oxidation." *Journal of Catalysis*, Vol 154(1), pp.98-106, (1995).

[93] Hummers Jr, W.S. and Offeman, R.E. "Preparation of graphitic oxide." *Journal of the american chemical society*, Vol 80(6), pp.1339-1339, (1958).

[94] Zhang, X., Song, X., Gao, S., Xu, Y., Cheng, X., Zhao, H. and Huo, L. "Facile synthesis of yolk–shell MoO_2 microspheres with excellent electrochemical performance as a Li-ion battery anode." *Journal of Materials Chemistry A*, Vol 1(23), pp.6858-6864, (2013)

[95] Zhang, X., Huang, X., Xue, M., Ye, X., Lei, W., Tang, H. and Li, C. "Hydrothermal synthesis and characterization of 3D flower-like MoS2 microspheres." *Materials Letters*, Vol 148, pp.67-70, (2015).

[96] Wang, X., Zhang, Z., Chen, Y., Qu, Y., Lai, Y. and Li, J. "Morphology-controlled synthesis of MoS_2 nanostructures with different lithium storage properties." *Journal of alloys and compounds*, Vol 600, pp.84-90, (2014).

[97] Paul, K.K., Sreekanth, N., Biroju, R.K., Narayanan, T.N. and Giri, P.K. "Solar light driven photoelectrocatalytic hydrogen evolution and dye degradation by metal-free few-layer MoS_2 nanoflower/TiO_2 (B) nanobelts heterostructure." *Solar Energy Materials and Solar Cells*, Vol 185, pp.364-374, (2018).

[98] Du, G., Guo, Z., Wang, S., Zeng, R., Chen, Z. and Liu, H. "Superior stability and high capacity of restacked molybdenum disulfide as anode material for lithium ion batteries." *Chemical communications*, Vol 46(7), pp.1106-1108, (2010)

[99] Akl, A.A. and Hassanien, A.S. "Microstructure and crystal imperfections of nanosized CdS_xSe_{1-x} thermally evaporated thin films." *Superlattices and Microstructures*, Vol 85, pp.67–81, (2015).

[100] Ma, L., Xu, L., Xu, X., Zhou, X., Luo, J. and Zhang, L."Cobalt-doped edge-rich MoS_2/nitrogenated graphene composite as an electrocatalyst for hydrogen evolution reaction." *Materials Science and Engineering: B*, Vol 212, pp.30–38, (2016).

[101] Fan, Q. "A new method of calculating interplanar spacing: the position-factor method." *Journal of Applied Crystallography*, Vol 45(6), pp.1303–1308, (2012).

[102] Tang, G., Wang, Y., Chen, W., Tang, H. and Li, C. "Hydrothermal synthesis and characterization of novel flowerlike MoS_2 hollow microspheres." *Materials Letters*, Vol 100, pp.15-18, (2013).

[103] Zhou, R., Han, C.J. and Wang, X.M."Hierarchical MoS_2-coated three-dimensional graphene network for enhanced supercapacitor performances." *Journal of Power Sources*, Vol 352, pp. 99–110, (2017).

[104] Li, X., Zhang, L., Zang, X., Li, X. and Zhu, H. "Photo-promoted platinum nanoparticles decorated MoS2@ graphene woven fabric catalyst for efficient hydrogen generation." *ACS Applied Materials & Interfaces*, Vol 8(17), pp.10866-10873, (2016).

[105] Gigot, A., Fontana, M., Serrapede, M., Castellino, M., Bianco, S., Armandi, M., Bonelli, B., Pirri, C.F., Tresso, E. and Rivolo, P. "Mixed 1T–2H phase MoS_2/reduced graphene oxide as active electrode for enhanced supercapacitive performance." *ACS Applied Materials & Interfaces*, Vol 8(48), pp. 32842–32852, (2016).

[106] Ho, W., Yu, J. C., Lin, J., Yu, J., and Li, P."Preparation and Photocatalytic Behavior of MoS_2 and WS_2 Nanocluster Sensitized TiO_2." *Langmuir*, Vol 20(14), pp. 5865–5869, 2004.

[107] Thakur, A.K., Deshmukh, A.B., Choudhary, R.B., Karbhal, I., Majumder, M. and Shelke, M.V. "Facile synthesis and electrochemical evaluation of PANI/CNT/MoS_2 ternary composite as an electrode material for high performance supercapacitor." *Materials Science and Engineering: B*, Vol 223, pp.24-34, (2017).

[108] Soon, J.M. and Loh, K.P. "Electrochemical double-layer capacitance of MoS_2 nanowall films." *Electrochemical and Solid-State Letters*, Vol 10(11), pp.250, (2007).

[109] Zhang, H., Wei, J., Yan, Y., Guo, Q., Xie, L., Yang, Z., He, J., Qi, W., Cao, Z., Zhao, X. and Pan, P. "Facile and scalable fabrication of MnO_2 nanocrystallines and enhanced electrochemical performance of MnO_2/MoS_2 inner heterojunction structure for supercapacitor application." *Journal of Power Sources*, Vol 450, pp.227616, (2020).

[110] Patil, S., Harle, A., Sathaye, S. and Patil, K. "Development of a novel method to grow mono-/few-layered MoS_2 films and MoS_2–graphene hybrid films for supercapacitor applications." *CrystEngComm*, Vol 16(47), pp.10845-10855, (2014).

[111] Islam, M.R., Pias, S.N.S., Alam, R.B. and Khondaker, S.I. "Enhanced electrochemical performance of solution-processed single-wall carbon nanotube reinforced polyvinyl alcohol nanocomposite synthesized via solution-cast method." *Nano Express*, Vol 1(3), pp.030013, (2020).

[112] Savjani, N., Lewis, E.A., Bissett, M.A., Brent, J.R., Dryfe, R.A., Haigh, S.J. and O'Brien, P. "Synthesis of Lateral Size-Controlled Monolayer 1H-MoS_2@Oleylamine as Supercapacitor Electrodes." *Chemistry of Materials*, Vol 28(2), pp.657-664, (2016).

[113] Chen, Y., Ma, W., Cai, K., Yang, X. and Huang, C. "In situ growth of polypyrrole onto three-dimensional tubular MoS_2 as an advanced negative electrode material for supercapacitor." *Electrochimica Acta*, Vol 246, pp.615-624, (2017).

[114] Chodankar, N.R., Gund, G.S., Dubal, D.P. and Lokhande, C.D. "Alcohol mediated growth of α-MnO_2 thin films from $KMnO_4$ precursor for high performance supercapacitors." *RSC Advances*, Vol 4(106), pp.61503-61513, (2014).

[115] Bissett, M.A., Kinloch, I.A. and Dryfe, R.A. "Characterization of MoS_2–graphene composites for high-performance coin cell supercapacitors." *ACS applied materials & interfaces*, Vol 7(31), pp.17388-17398, (2015).

[116] Ramalingam, R.J., Konikkara, N., Al-Lohedan, H., Al-Dhayan, D.M., Kennedy, L.J., Basha, S.K. and Sayed, S.R. "Synthesis of MoS_2 nanoparticle deposited graphene/mesoporous MnO_x nanocomposite for high performance super capacitor application." *international journal of hydrogen energy*, Vol 43(36), pp.17121-17131, (2018).

[117] Majumder, M., Choudhary, R.B., Thakur, A.K. and Karbhal, I. "Impact of rare-earth metal oxide (Eu_2O_3) on the electrochemical properties of a polypyrrole/CuO polymeric composite for supercapacitor applications." *RSC advances*, Vol 7(32), pp.20037-20048, (2017).

[118] Muniraj, V.K.A., Kamaja, C.K. and Shelke, M.V. "$RuO_2 \cdot nH_2O$ nanoparticles anchored on carbon nano-onions: an efficient electrode for solid state flexible electrochemical supercapacitor." *ACS Sustainable Chemistry & Engineering*, Vol 4(5), pp.2528-2534, (2016).

[119] Chen, Y., Ma, W., Cai, K., Yang, X. and Huang, C. "In situ growth of polypyrrole onto three-dimensional tubular MoS2 as an advanced negative electrode material for supercapacitor." *Electrochimica Acta*,Vol 246, pp.615-624, (2017).

[120] Heydari, H., Abdouss, M., Mazinani, S., Bazargan, A.M. and Fatemi, F. "Electrochemical study of ternary polyaniline/MoS_2−MnO_2 for supercapacitor applications." *Journal of Energy Storage*, Vol 40, pp.102738, (2021).

[121] Xie, Y. and Du, H. "Electrochemical capacitance of a carbon quantum dots–polypyrrole/titania nanotube hybrid." *Rsc Advances*, Vol 5(109), pp.89689-89697, (2015).

[122] Zhong, C., Deng, Y., Hu, W., Qiao, J., Zhang, L. and Zhang, J. "A review of electrolyte materials and compositions for electrochemical supercapacitors." *Chemical Society Reviews*, Vol 44(21), pp.7484-7539, (2015).

[123] Bhagwan, J., Sahoo, A., Yadav, K.L. and Sharma, Y. "Porous, one dimensional and high aspect ratio Mn_3O_4 nanofibers: fabrication and optimization for enhanced supercapacitive properties." *Electrochimica Acta*, Vol 174, pp.992-1001, (2015).

[124] Liu, Y., Wu, Q., Liu, L., Manasa, P., Kang, L. and Ran, F. "Vanadium nitride for aqueous supercapacitors: a topic review. *Journal of materials chemistry A*, Vol 8(17), pp.8218-8233, (2020).

[125] Portet, C., Taberna, P.L., Simon, P. and Laberty-Robert, C. "Modification of Al current collector surface by sol–gel deposit for carbon–carbon supercapacitor applications." *Electrochimica Acta*, Vol 49(6), pp.905-912, (2004).

[126] Chen, Y., Zhu, X., Yang, D., Wangyang, P., Zeng, B. and Sun, H. "A novel design of poly (3, 4-ethylenedioxythiophene): poly (styrenesulfonate)/molybdenum disulfide/poly (3, 4-ethylenedioxythiophene) nanocomposites for fabric micro-supercapacitors with favourable performances." *Electrochimica Acta*, Vol 298, pp.297-304, (2019).

[127] Rafiee, E., Farzam, M., Golozar, M.A. and Ashrafi, A. "An investigation on dislocation density in cold-rolled copper using electrochemical impedance spectroscopy." *International Scholarly Research Notices*, (2013).

[128] Chen, Y., Ma, W., Cai, K., Yang, X. and Huang, C. "In situ growth of polypyrrole onto three-dimensional tubular MoS_2 as an advanced negative electrode material for supercapacitor." *Electrochimica Acta*, Vol 246, pp.615-624, (2017).

[129] Ma, L., Xu, L., Xu, X., Zhou, X., Luo, J. and Zhang, L. "Cobalt-doped edge-rich MoS2/nitrogenated graphene composite as an electrocatalyst for hydrogen evolution reaction." *Materials Science and Engineering: B*, Vol 212, pp.30-38, (2016).

[130] Jia, Y., Lin, Y., Ma, Y. and Shi, W. "Hierarchical MnS_2-MoS_2 nanotubes with efficient electrochemical performance for energy storage." *Materials & Design*, Vol 160, pp.1071-1079, (2018).

[131] Lamiel, C. and Shim, J.J. "Hierarchical mesoporous graphene@ Ni-Co-S arrays on nickel foam for high-performance supercapacitors." *Electrochimica Acta*, Vol 161, pp.351-357, (2015).

[132] Li, D., Zhou, W., Zhou, Q., Ye, G., Wang, T., Wu, J., Chang, Y. and Xu, J. "Transparent 1T-MoS2 nanofilm robustly anchored on substrate by layer-by-layer self-assembly and its ultra-high cycling stability as supercapacitors." *Nanotechnology*,Vol 28(39), pp.395401, (2017).

[133] Islam, M.R. and Mollik, S.I. "Enhanced electrochemical performance of flexible and eco-friendly starch/graphene oxide nanocomposite." *Heliyon*, Vol 6(10),pp.e05292, (2020).

[134] Huang, F., Meng, R., Sui, Y., Wei, F., Qi, J., Meng, Q. and He, Y. "One-step hydrothermal synthesis of a CoS_2@ MoS_2 nanocomposite for high-performance supercapacitors." *Journal of Alloys and Compounds*, Vol 742, pp.844-851, (2018).

[135] Wang, L., Ma, Y., Yang, M. and Qi, Y. "Titanium plate supported MoS_2 nanosheet arrays for supercapacitor application." *Applied Surface Science*, Vol 396, pp.1466-1471, (2017).

[136] Huang, K.J., Wang, L., Liu, Y.J., Liu, Y.M., Wang, H.B., Gan, T. and Wang, L.L. "Layered MoS_2–graphene composites for supercapacitor applications with enhanced capacitive performance." *International journal of hydrogen energy*, Vol 38(32), pp.14027-14034, (2013).